# Single-cell roadmap of cardiac differentiation identifies roles for ZNF711 and retinoic acid in balanced epicardial and cardiomyocyte lineage commitment


## AUTHORS

**Rebecca R. Snabel[1,4], Carla Cofiño-Fabrés[2,4], Marijke Baltissen[3], Verena Schwach[2], Robert Passier[2,5]*, Gert Jan C. Veenstra[1,5]***

[1]Department of Molecular Developmental Biology, Radboud Institute for Molecular Life Sciences, Faculty of Science, Radboud University, Nijmegen, The Netherlands

[2]Department of Bioengineering Technologies, Applied Stem Cell Technologies Group, TechMed Centre, University of Twente, Enschede, The Netherlands

[3]Department of Molecular Biology, Radboud Institute for Molecular Life Sciences, Faculty of Science, Oncode Institute, Radboud University, Nijmegen, the Netherlands

[4]These authors contributed equally

[5]Senior author

*Correspondence: gertjan.veenstra@ru.nl, robert.passier@utwente.nl



## SUMMARY

Stem cell-based models of human heart tissue and cardiac differentiation employ monolayer and 3D organoid cultures with different properties, cell type composition, and maturity. We constructed a single-cell roadmap of atrial and ventricular differentiation conditions, enabling direct comparisons of monolayer, cardiac embryoid body, and engineered heart tissue trajectories. Using a multiomic approach and gene-regulatory network inference, we focused on the regulators of the epicardial, atrial and ventricular cardiomyocyte lineages. We identified *ZNF711* as a regulatory switch and safe-guard for cardiomyocyte commitment. We show that *ZNF711* ablation prevents cardiomyocyte differentiation in the absence of retinoic acid, causing progenitors to be diverted more prominently to epicardial and other lineages. Retinoic acid rescues this shift in lineage commitment and promotes atrial cardiomyocyte differentiation, showing an interplay between *ZNF711* and retinoic in cardiac lineage commitment.


## HIGHLIGHTS

- We present an atlas of cardiac differentiation under different culture conditions, showing progenitor trajectories and cell states reminiscent of the fetal heart.
- Multiome and chromatin accessibility analysis identified candidate regulators of cardiomyocyte and non-cardiomyocyte lineages.
- Distinct trajectories of lineage commitment and differentiation under different culture conditions shows plasticity of first and second heart field progenitors and different ratios of cardiomyocyte and non-myocyte lineages.
- ZNF711 is required for balanced commitment to epicardial and ventricular cardiomyocyte lineages. Retinoic acid rescues a requirement for ZNF711 in cardiomyocyte differentiation, promoting both atrial cardiomyocyte and epicardial differentiation.

Graphical Abstract

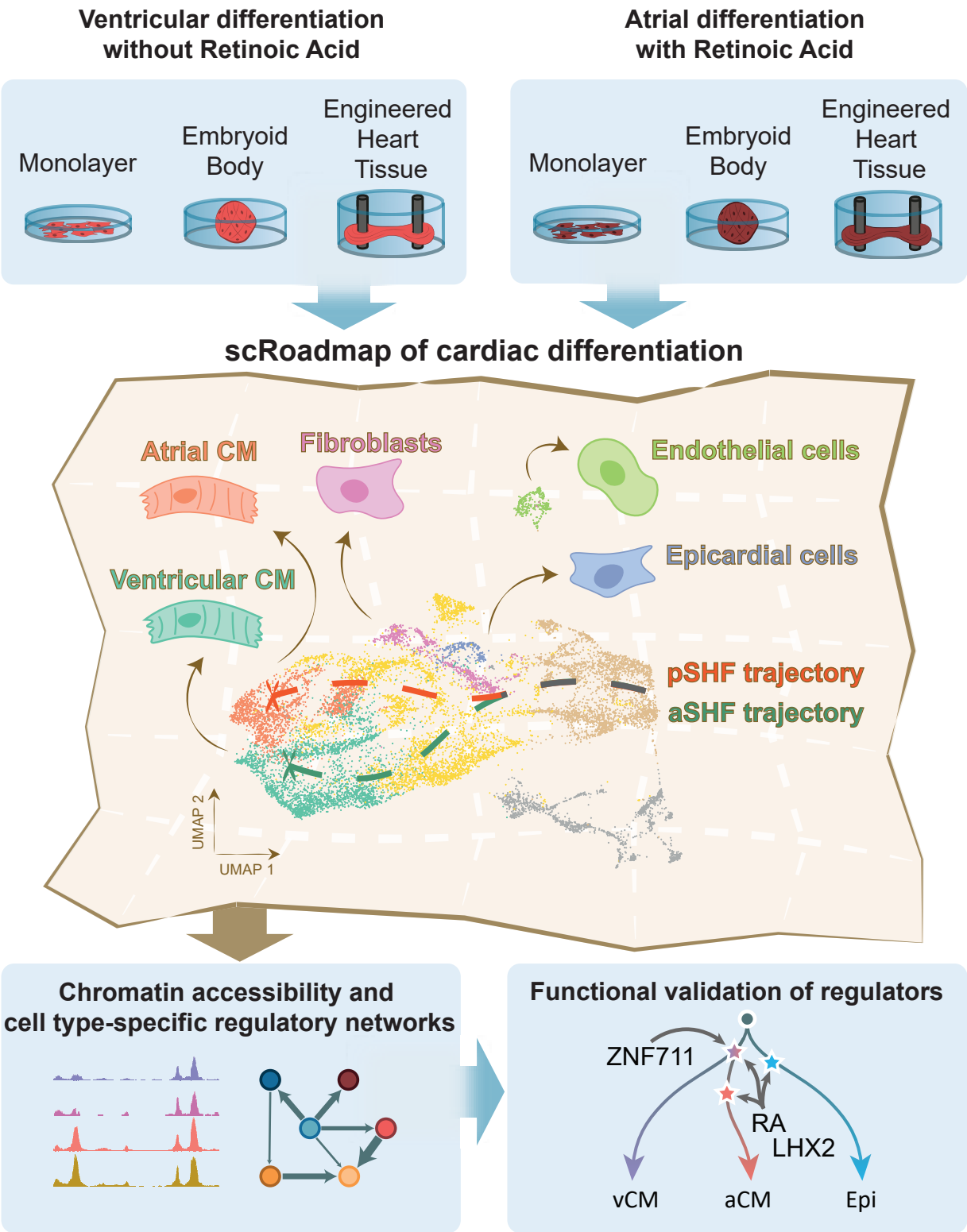

## INTRODUCTION

The first precursor cells of the heart emerge during early gastrulation when the three germ layers of the embryo are formed (Lescroart et al., 2014; Saga et al., 1999). These progenitor cells reside within the splanchnic lateral mesoderm in spatially segregated populations, notably the first and the second heart field (FHF and SHF), which together will form the cardiac crescent (Buckingham et al., 2005). These progenitor states and their lineage contributions have been studied using single-cell omics approaches in mouse embryonic tissues, as reviewed recently (Lescroart & Zaffran, 2022; Sendra et al., 2021; Tyser, 2023). The lineages of the FHF primarily populate the left ventricle and part of the atria. The SHF is divided into an anterior and posterior section (aSHF and pSHF), which are transcriptionally distinct and contribute to different parts of the developing heart (Lescroart et al., 2018). The aSHF forms the right ventricular myocardium and outflow tract of the heart, whereas progenitors of the pSHF commit to the atrial lineage under the influence of retinoic acid (RA) signaling (Protze et al., 2019). Reports on cardiac development in humans start at five weeks of gestation, when the heart already features multiple chambers (Asp et al., 2018; Cui et al., 2019; Devalla et al., 2015; Farah et al., 2024; Sahara et al., 2019). By that time, the multipotent cardiac progenitors have produced the cardiomyocyte, endothelial, epicardial and smooth muscle lineages and have built a myocardium that forms the atria and ventricles (Protze et al., 2019). Very little is known about the earliest stages and distinctive lineage choices of human cardiac development *in vivo* (Tyser et al., 2021; Zeng et al., 2023).

Human pluripotent stem cells (hPSC) offer an immense potential to differentiate many cell types *in vitro*, thus presenting a relevant alternative in mimicking the earlier steps of human tissue development (Takahashi et al., 2007; Thomson et al., 1998; Yu et al., 2007). Various culture models have been established to obtain cardiomyocytes (CMs) (Burridge et al., 2012; Devalla & Passier, 2018; Mummery et al., 2012), with variations including an early step of retinoic acid (RA) treatment to enrich for atrial CMs (aCMs) (Devalla et al., 2015; Lee et al., 2017; Schwach et al., 2022; Zhang et al., 2010) or epicardial derivatives (Guadix et al., 2017; Hofbauer et al., 2021a; Meier et al., 2023). Over time, the cardiac cultures have increased in complexity (e.g. from two- to three-dimensional cultures and combinations of different cell types) leading to advanced maturity of the cardiomyocytes and simultaneous development of a dynamic pool of cardiac cell types (DeLaughter et al., 2016; Kannan et al., 2021).

Single-cell transcriptomic studies have elucidated the differentiation processes of hPSCs towards CMs (Ameen et al., 2022; Churko et al., 2018; Friedman et al., 2018; Grancharova et al., 2021; Hofbauer et al., 2021b; Lewis-Israeli et al., 2021; Meier et al., 2023; Mononen et al., 2020; Ruan et al., 2019; Sahara et al., 2019; Zawada et al., 2023). Several of these studies highlighted the presence of non-

74 myocyte subpopulations within the culture (Churko et al., 2018; Friedman et al., 2018; Mononen et al.,
75 2020), while others shed light on the specification of particular cardiomyocyte subtypes, such as atrial,
76 right and left ventricular CMs, and node-like CMs (Funakoshi et al., 2021; Pezhouman et al., 2021;
77 Wiesinger et al., 2022; Yang et al., 2022). However, very little is known about how cardiac multipotent
78 progenitors give rise to different cardiomyocyte and non-myocyte lineages, and how this is regulated.
79 Hence, there is a need for disentangling the gene regulatory networks (GRNs) of cardiac development
80 as the cells commit to specific lineages, and how they govern cardiac differentiation in the context of
81 *in vitro* culture conditions. Understanding these mechanisms will aid in the advancement of cardiac
82 hPSC models and their ability to more accurately model cardiovascular development and heart disease.
83 Here we present a detailed comparison of *in vitro* cardiac differentiation conditions from hPSCs
84 using single-cell transcriptomic (RNA) and chromatin accessibility (ATAC) data, which we used to
85 construct a roadmap of atrial and ventricular multilineage differentiation. We used a combination of
86 monolayer, embryoid body (EB) and engineered heart tissue (EHT) cultures to compare their cellular
87 compositions and differentiation stages. In addition, we used RA to compare multilineage
88 differentiation in atrial and ventricular cultures. Direct comparisons between the cardiac models
89 revealed subpopulations resembling *in vivo* cell states and identified transcriptional regulators at the
90 onset of lineage commitment. The integrative multiomic approach led to the identification of *ZNF711*,
91 and the interplay of this zinc finger with RA in balancing commitment to the cardiomyocyte and
92 epicardial lineages.

93 **RESULTS**

94 **Cardiomyocyte differentiation methods produce cardiac cell states found in the human fetal heart**

95 To compare the early steps of cardiac lineage development, we differentiated dual fluorescent *NKX2-*
96 *5*$^{EGFP/+}$ and *COUP-TFII* (*NR2F2*)$^{mCherry/+}$ hPSCs to CMs under cardiomyocyte monolayer (Mon) and cardiac
97 EB conditions, with or without RA (Methods, Fig. 1A, Supplementary Fig. S1A). We and others showed
98 previously that RA redirects differentiation towards aCMs (Devalla et al., 2015; Schwach et al., 2017,
99 2022; Zhang et al., 2010), which occurs at high efficiency as evaluated by fluorescence activated cell
100 sorting (Supplementary Fig. S1B). At day 14, CMs of these cultures were further matured for an
101 additional 12 days (m12) until day 26, by either generating 3D engineered heart tissues (EHT) (Birket et
102 al., 2015; Ribeiro et al., 2022), or replating to monolayer as a control for the changes that occur in the
103 EHTs, both with the addition of cardiomyocyte maturation medium (Supplementary Fig. S1C). The atrial
104 and ventricular CMs expressed the expected regional markers (NR2F2 and MYL2 respectively; Fig. 1B)
105 in addition to general cardiomyocyte markers (MYL7, ACTN2; Supplementary Fig. S1D), while displaying
106 typical action potential profiles, with higher frequencies and shorter action potential duration times in
107 aCMs (Supplementary Fig. S1E). Continued culture of the CMs in the EHT model enhanced their

respective identities, as shown by immunohistochemistry of aCM and vCM-specific markers (Supplementary Fig. S1F).

To produce a detailed map of how cardiac progenitors give rise to cardiomyocytes and other cardiac cell types, we performed single-cell RNA sequencing on samples of different culture methods and time points (Fig. 1A, C). We used a 384-well plate-based platform (SORT-Seq) because of the flexibility it offers in experimental design and it facilitates the capture of many time points and different culture conditions (Hashimshony et al., 2016; Muraro et al., 2016). Particularly, we captured cells at the mesodermal stage (day 4-5), cardiac progenitors (day 7-9), cells committed to the CM fate (day 10-14) and definitive CMs (day 18-26). This resulted in a single-cell landscape covering different protocols and time points with a total of 12,706 cells after filtering for quality (Methods, Supplementary Fig. S2A-B). Known cardiac markers for different stages of development were evaluated for their overall expression patterns over time (Supplementary Fig. S2C), indicating a decrease in mesodermal markers (*MIXL1*, *PDGFRA*), alongside an increase in cardiac progenitor markers (*NKX2-5*, *MEF2C*), followed by structural CM genes (*TNNT2*, *MYL7*) in combination with specific atrial (*KCNA5*, *KCNJ3*, *VSNL1*) or ventricular (*MYL2*, *MYH7*, *VCAM1*) CM genes (Supplementary Fig. S2D).

To predict which cells of the different culture methods represent a similar biological state, we integrated the data using an unsupervised selection of mutual cell pairings across the multiple culture experiments (Supplementary Fig. S2E-F) (Haghverdi et al., 2018; Stuart et al., 2019). This resulted in an integrated *in vitro* cardiac differentiation atlas or roadmap, in which a chronological progression of time points and cell states was observed, while resolving distinctions between the atrial and ventricular lineage (Fig. 1C). Comparing the end states of the differentiation culture methods revealed a clear shift of the definitive CM populations between monolayer and EHT cultures, corresponding to further maturation upon culturing as 3D EHTs (Supplementary Fig. S2G). To annotate the different cell states across the different cultures and time points, we compared the cell clusters with an integrated dataset of human fetal heart development (Asp et al., 2019; Cui et al., 2019) (Supplementary Fig. S3 and S4A-D). This *in vivo* comparison revealed that from day 8 onward and specifically in the EB method, clusters matching cardiac fibroblasts and smooth muscle cells were present (clusters 15-16), alongside clusters comparable to endothelial and epicardial cells (respectively clusters 17 and 22) (Fig. 1D, Supplementary Fig. S4A-D). Fibroblasts (cluster 16) were relatively abundant in the EHT model, but epicardial-like cells (cluster 22) were not (Supplementary Fig. S4B-D). This decrease is likely linked to the dissociation of the EBs and sorting and selection of the cells for the EHTs with an 80:20 ratio of CM and non-CM cells (Fig. 1A). Expression of well-known marker genes, such as *FBN1* for fibroblasts, *WT1* for epicardium and *TAGLN2* for smooth muscle cells (Fig. 1E-G), further confirmed the presence of these non-myocyte cell types. Lastly, one set of clusters (clusters 10, 13, 18 and 25) of cells present in the EB cultures of both lineages (Supplementary Fig. S4D), was found enriched for markers of endoderm-committed cell types,

143 such as early foregut progenitors (Supplementary Fig. S6). The definitive endoderm and foregut
144 derivatives can contribute to epicardial and myocardial lineage development (Branco et al., 2022).
145 Overall, these data highlight the broad lineage potential in both ventricular and atrial EB cultures (Fig.
146 1D). In addition, we found that a population of cells consisting of non-CM and early CM progenitors,
147 were marked by high expression of *COL3A1*, and that this expression is inversely related to that of
148 *TNNT2* in the CM lineage (Fig. 1H-I). This *COL3A1*-high population shows a different abundance in the
149 cardiac cultures, raising the possibility that the balance of lineage commitment of multipotent
150 progenitors towards CM and non-CM identities is affected by the culture method.
151
152 **Early trajectories show expression patterns mimicking *in vivo* development**
153 To study the relationship between *COL3A1*-high progenitors and the CM and non-CM lineages, we
154 performed cell trajectory analysis for each culture method from early time points up to day 14 (Fig. 2A-
155 F). This revealed the progression of cardiac progenitors expressing *COL3A1* (Fig. 2G-I) to epicardial cells
156 in atrial and ventricular EBs (Fig. 2D-F, Supplementary Fig. S6) and *TNNT2*-positive CMs in all cultures
157 (Fig. 2J-L). The epicardial trajectory is supported by the presence of cells expressing *ISL1, HAND1* and
158 *BNC2*, markers of the juxta-cardiac field or pre-epicardial progenitor state (Supplementary Fig. S6A-D).
159 This population is continuous with cells that are negative for *ISL1* and *NKX2-5*, while expressing
160 epicardial markers *WT1, SFRP5* and *ITGA8* (Supplementary Figs. S6B, E-G and S7F). In each of the early
161 cultures, the *COL3A1*-high state was present, although this was more pronounced in the atrial EBs
162 treated with RA (Fig. 2I). In the ventricular monolayer culture, CM progenitors can go through either a
163 high or a low *COL3A1*-expression state before acquiring the CM identity (Fig. 2G, J). In EBs, the
164 progenitors are routed almost exclusively through a *COL3A1*-high state (Fig. 2H-I), but the *COL3A1*-high
165 population is much expanded in the RA-treated atrial EB culture conditions. In most progenitors
166 present in the EBs, *COL3A1* appears to be co-expressed with the second heart field (SHF) progenitor
167 marker *ISL1*, as shown before (Mononen et al., 2020). There is no co-expression, however, in the
168 epicardial population, which does express *COL3A1* but not *ISL1* (Fig. 2H-I, Supplementary Fig. S6B). This
169 is in line with previously described dynamics of *ISL1* expression during epicardial lineage progression
170 (Meier et al., 2023).
171 To establish if other *in vivo* developmental stages were recapitulated *in vitro*, we checked the
172 expression of SHF and FHF markers across culture methods and time points (Supplementary Fig. S7A-
173 B). Several SHF markers were upregulated over the course of differentiation both in the atrial and
174 ventricular lineage (*HAND2*, *ISL1* and *FOXC1*; Supplementary Fig. S7B). In the atrial EB culture
175 conditions, an increase of *TBX5* expression occurred directly after a transient increase of *HOXA1*
176 expression (Roux et al., 2016; Steimle & Moskowitz, 2017; Sweat et al., 2023) points (Supplementary

177 Fig. S7B). This particular expression profile is consistent with the expected posterior SHF (pSHF) identity
178 (Protze et al., 2019). Other examples of pSHF markers that increased in the atrial EBs are *FOXF1, TBX18*
179 and *OSR1* (Hill et al., 2019; Meilhac & Buckingham, 2018; Steimle & Moskowitz, 2017) (Supplementary
180 Fig. S7C-D). On the other hand, the vCM cultures showed limited expression of *TBX5* in comparison to
181 the aCM cultures points (Supplementary Fig. S7B), while *FGF8* and *FGF10* increased alongside an early
182 expression of *SIX1*, indicative of anterior SHF identity (aSHF) (Itoh et al., 2016; Yang et al., 2022)
183 (Supplementary Fig. S7E). By examining the identity of the CMs from day 14 onwards (Supplementary
184 Fig. S2D), we observed a higher expression of *MYL2,* together with the expression of *HAND2* and
185 *SEMA3C* (Supplementary Fig. S7B, G) in the ventricular clusters (derived from both EB and monolayer
186 cultures), associated with an outflow tract (OFT)-like or right ventricle CM identity (Rana et al., 2014;
187 Yang et al., 2022). These findings suggest SHF progenitors develop in these cardiac cultures, with an
188 aSHF identity in the ventricular culture and a posteriorizing effect of RA (pSHF) in the atrial EB culture.
189 The ventricular cultures additionally expressed the FHF marker *HAND1* (Supplementary Fig. S8B),
190 consistent with contributions to left ventricular CM. Collectively, these results outline multiple routes
191 towards a cardiomyocyte fate, one with relatively low *COL3A1* expression on a mixed aSHF-FHF
192 trajectory towards vCMs, and another of *COL3A1*-high expression progressing towards aCMs derived
193 from a more posteriorized SHF lineage, a dynamic that is driven by treatment with RA (Supplementary
194 Fig. S7D). Interestingly, epicardial marker genes such as *SFRP5* (Fujii et al., 2017), overlapped with
195 *COL3A1* in the non-cardiomyocyte branches in EB cultures, irrespective of RA-induced posteriorization
196 of the SHF (Supplementary Fig. S6F-G and Fig. S7F). These data document the dynamic re-routing of
197 progenitors along developmental trajectories depending on the culture method, raising the question
198 what molecular mechanisms are underlying this plasticity of multilineage cardiac differentiation.
199

200 **Identification of candidate cardiac regulators by integrative multiomic analysis**

201 We focused first on the influence of RA on lineage specification in EBs, as it provides a major switch for
202 atrial versus ventricular CM lineage specification in these cultures, in the presence of a relatively stable
203 number of non-CM cell types (cf. Fig. 1D). To study lineage-specific transcription factor expression
204 patterns, an EB subset of the atlas was generated to perform differential-expression testing over time
205 on CM-committed cell clusters (Fig. 3A, Supplementary Fig. S8A-D). This analysis outlined several
206 known CM-specification markers, such as ventricular *IRX3* and *HEY2,* and atrial *MEIS2*, *NR2F2/*1 and
207 *HEY1*. Additionally, atrial-enriched expression was found for *LHX2, ZNF711* and *ZNF503* (Supplementary
208 Fig. S8E-G), genes that are not known for their role in CM lineage commitment. Since RA was added to
209 the atrial cultures for 24 hours on day 4, 'early' genes can be identified that are only transiently induced

210 by RA (for example *HOXA1*), whereas 'long-term' genes (for example *LHX2*, *ZNF711* and *ZNF503*) are
211 induced with delayed dynamics (Supplementary Fig. S8D, H).
212 To examine the role of these and other transcription factors at the level of chromatin accessibility,
213 we generated an orthogonal single-nucleus multiomic dataset (snRNA-seq and snATAC-seq) of atrial
214 and ventricular EBs at the onset of lineage commitment (day 8, Fig. 3A). Dimensionality reduction and
215 clustering of the transcriptome modality of the data led to the identification of the cell states we
216 identified before, with a *KCNJ3* and *NR2F1*-positive population of early aCMs, vCMs expressing *MYL7*
217 and *MYH6,* a *GRHL2* and *CDH1*-positive population of epicardial cells, and an endothelial cluster
218 marked by *KDR* (or *FLK1*) and *FLI1* expression (Fig. 3B-C, Supplementary Fig. S9A-C). Subclusters
219 observed within the CM clusters (labeled vCM2 and aCM2) were marked by gene expression associated
220 with different cell cycle phases (Supplementary Fig. S9B-C). Correlation of the multiome clusters with
221 day 8 EB clusters of the atlas, revealed similarities of the 'other' cluster (Fig. 3B) with the endoderm
222 clusters of the atlas (Supplementary Fig. S10A-C), while also being marked by fibroblast genes *FGF13*
223 and *SCN7A* (Supplementary Fig. S9C).
224 With the clusters outlined in the multiomic data based on gene expression, peak calling and
225 differential peak accessibility analysis was performed on the chromatin accessibility modality of the
226 dataset. At this early stage of lineage commitment and RA-dependent change, quantitative differences
227 in accessibility between cell clusters were observed for relatively few genes (Fig. 3D, Supplementary
228 Fig. S9D). We then examined the transcription factor motifs correlating with differences in chromatin
229 accessibility between cell clusters ('motif activity', Methods), which identified motifs linked to
230 important cardiac regulators (Fig. 3E, Supplementary Table S1A-B). For example, the motifs of RA-
231 receptor (RARB) and HOXB1 are associated with chromatin accessibility in atrial CMs (aCM and aCM2
232 clusters), proteins known to be induced by RA and to be implicated in pSHF development (Roux et al.,
233 2016). The motifs for IRX3 and SRF, important for aSHF and CM differentiation (Gaborit et al., 2012;
234 Guo & Pu, 2020; Kim et al., 2016; Yang et al., 2022), were associated with the vCM clusters. Other
235 examples include the WT1 and ERG1 motifs enriched in the epicardial cluster (Marques et al., 2022;
236 Meier et al., 2023; von Gise et al., 2011), the GATA2 motif in endothelial cells (Kanki et al., 2011), and
237 motifs for HNF4A and SOX17 in the endoderm cluster (Hanawa et al., 2017; Kanai-Azuma et al., 2002;
238 Séguin et al., 2008). A motif for ZNF711 showed activity in the endothelial, epicardial and aCM clusters
239 (Fig. 3E).
240

241 **Gene regulatory network acting downstream of retinoic acid points to LHX2 and ZNF711 as novel**
242 **regulators of interest**

243 To understand the transcriptional regulation driving CM specification in these stages of cardiac
244 development, we predicted the CM-specific gene regulatory networks (GRNs) utilizing scANANSE, a

245 recently developed tool for identification and prioritization of key transcription factors involved in cell
246 fate determination (Smits et al., 2023; Xu et al., 2021). In short, scANANSE prioritizes transcription
247 factors by integration of chromatin accessibility (sequence motif content) and transcriptome data,
248 inferring a differential network between two biological states. The differential network allows
249 scANANSE to prioritize factors for their inferred ability to "reprogram" cells from one biological state
250 to another. The predicted aCM network (Supplementary Table S1C), highlighted many regulators known
251 for their role in cardiac development and regulation of cardiac progenitors from the pSHF, like TBX18,
252 MEIS2 and NR2F2 (Lescroart & Zaffran, 2018; Quaranta et al., 2018). The vCM network included
253 multiple known CM-regulators, such as TBX20, MEF2A/C and NKX2-5, but also HEY2, a regulator
254 particular to the ventricular subtype (Buckingham, 2015; Churko et al., 2018) (Supplementary Table
255 S1D). For the non-CM clusters which consisted of cells from both culture conditions, we compared the
256 cell type specific network to an average network of all cells together (Methods). Top influential factors
257 identified this way, for the epicardial network included *GRHL2*, *TFAP2A*, *BACH2*, for endothelial network
258 these included *ERG*, *ETS1*, *FLI1*, *ELK3*, and for the endoderm network *RFX6*, *GATA3*, *HNF4A* and *HNF4G*
259 (Supplementary Table S1E-G).

260 Subsequently, we used the temporal gene expression information from our transcriptome atlas
261 (Supplementary Fig. S8H), to infer a temporal regulatory hierarchy within the aCM network. Based on
262 these expression dynamics within the top-ranked network of transcription factors, RA receptor beta
263 (RARB) emerged as the regulatory starting point (Fig. 3F), consistent with the use of RA to trigger atrial
264 lineage commitment. RARB is predicted to regulate multiple well-known pSHF genes (i.e. *MEIS2*, *TBX18*,
265 *NR2F2* and *FOXC1*). Top-regulators encoded among the long-term RA-induced genes are GATA6, MEIS2,
266 PBX3, PBX1 and NR2F2 (Fig. 3G). The predicted regulatory interactions of seven genes of interest
267 (*COL3A1, KCNA5, TNNT2, SFRP5, MYL7, KCNJ3, HAND2*) suggest that most targets can be regulated by
268 RARB directly, whereas *COL3A1* and *KCNA5* may be regulated further downstream in the network by
269 the long-term regulators.

270 Among the influential factors of the aCM network, also ZNF711 and LHX2 were identified. Multiple
271 influential factors were predicted to regulate *ZNF711* in the aCM network (Fig. 3H), among which
272 known pSHF factors TBX5, HEY1, MEIS1/2 and NR2F1, but also factors more generally implicated in
273 cardiac development such as GATA4/6 (Xin et al., 2006). ZNF711 was predicted to regulate some of
274 these and other SHF regulators like *ISL1* and *FOXC1*, as well as general CM and aCM-specific markers
275 (i.e. *TNNT2*, *MYL7* and *NR2F2*, *MYL6*). Additionally, *ZNF503* was found downstream of ZNF711 in the
276 aCM network. These findings were especially interesting since limited information is available regarding
277 the potential role of these zinc-finger proteins in cardiac development. The highly conserved *ZNF503*
278 protein has been shown to transcriptionally repress *GATA3* (Shahi et al., 2017) and to play a critical role
279 during embryonic development in mice and zebrafish (Boobalan et al., 2022; Nakamura et al., 2008;

280 Shahi et al., 2017). The predicted regulatory role of *ZNF711*, as well as the expression patterns of both
281 *ZNF711* and *ZNF503* in our data, prompted us to further investigate these transcription factors.
282

283 **Ablation of ZNF711 halts cardiomyocyte differentiation and favors the epicardial and endodermal**
284 **lineage**

285 We selected three genes (*LHX2*, *ZNF711* and *ZNF503*) to assess their roles in cardiac lineage
286 commitment. For each of these factors a CRISPR knockout (KO) was performed in the dual
287 NKX2.5$^{EGFP/+}$COUP-TFII(NR2F2)$^{mCherry/+}$ hPSC reporter line (Schwach et al., 2017), with KO efficiencies
288 over 70% each, both before and after cardiac EB differentiation (Supplementary Fig. S11A-B). KO hPSCs
289 were immediately differentiated in EB cultures over the course of 14 days towards the ventricular (non-
290 RA) and atrial (+RA) cardiac cell types. The efficiency of CM differentiation was assessed using NKX2-5-
291 GFP reporter expression (Fig. 4B). In the ventricular *ZNF711*-KO culture, reporter expression was
292 significantly lower compared to control, while this was not observed in the RA-treated (atrial) *ZNF711*-
293 KO EBs or in any of the other conditions. The lower CM differentiation efficiency in the ventricular
294 ZNF711-KO was accompanied by an increase in the abundance of NKX2-5-GFP-negative and NR2F2-
295 mCherry-positive fraction compared to control (Supplementary Fig. S11C), suggesting a shift in lineage
296 commitment.

297 A substantial differentiation defect in the ventricular culture was corroborated by transcriptome
298 analysis, which we performed for both the atrial and ventricular cardiac EB cultures of each KO at day
299 14 of differentiation. The strongest changes in gene expression were detected in the *ZNF711*- and *LHX2*-
300 ablated cultures relative to controls (Supplementary Fig. S11E, Supplementary Table S2A-D). To explore
301 changes in cell type commitment, sets of 200 marker genes per cell type were defined from the atlas
302 to calculate average cell type-specific marker expression levels per KO and culture condition (Fig. 4C).
303 This analysis uncovered that changes in cell lineage-specific markers was highly dependent on the
304 treatment with RA. The *ZNF711*-KO samples showed a significant decrease in both aCM and vCM
305 markers under ventricular conditions (Wilcoxon p-adjusted 2.7 x $10^{-9}$ and 2.2 x $10^{-11}$, respectively). In
306 RA-treated atrial cultures, however, vCM marker expression was not affected significantly, while the
307 expression of aCM markers increased significantly (Wilcoxon p-adjusted 7.8 x $10^{-5}$) and the expression
308 of aCM progenitor markers was reduced (Wilcoxon p-adjusted 2.6 x $10^{-11}$). In ventricular cultures,
309 definitive endoderm marker expression was increased (Wilcoxon p-adjusted 1 x $10^{-8}$), alongside
310 epicardial gene expression (Wilcoxon p-adjusted 4.6 x $10^{-3}$). The *ZNF711*-KO samples exhibited
311 significant downregulation of general cardiomyocyte markers (*TNNT2*: p-adjusted 1.1 x $10^{-16}$, *IRX4*: 6.2
312 x $10^{-16}$, *TBX20*: 1.3 x $10^{-10}$, *PLXNA4*: 6 x $10^{-8}$) (Fig. 4D, Supplementary Table S2B) and gene ontology terms
313 (Supplementary Table S2G) in the ventricular cultures. This was not observed in the RA-treated atrial
314 *ZNF711*-KO samples, in which upregulated genes were enriched for the terms *muscle cell differentiation*

315 and *muscle system process* (Supplementary Table S2G). This suggests that the inhibition of
316 cardiomyocyte differentiation observed in ventricular cultures, was rescued by RA in the atrial *ZNF711*-
317 KO cultures. To characterize this in more detail, *ZNF711*-KO up- and down-regulated genes were used
318 to calculate module scores in the single-cell *in vitro* atlas (Fig. 4E). The ventricular *ZNF711*-KO
319 downregulated targets (Fig. 4E, left panel) normally show high expression in all of the CM-committed
320 clusters within the atlas, whereas the ventricular *ZNF711*-KO upregulated genes are normally expressed
321 in the non-CM branches of the atlas (Fig. 4E, middle-left). These results were corroborated by the
322 increased NR2F2 protein levels measured in a NKX2-5-negative population (Supplementary Fig. S11D),
323 combined with increased expression levels of *COL3A1* and *SFRP5* (p-adjusted 0.029 and 0.019,
324 respectively) (Supplementary Table S2B) in these ventricular *ZNF711*-KO cultures compared to control,
325 indicating a shift in populations from CMs to non-CMs. Conversely, the atrial *ZNF711*-KO downregulated
326 genes were mostly expressed in the non-CM populations and CM progenitors (Fig. 4E, middle-right)
327 and upregulated genes showed specific expression in later CM differentiation stages of the atlas (Fig.
328 4E, right panel). These data show that *ZNF711*-KO hampered CM differentiation and increased both
329 progenitor and non-CM signatures in the absence of RA, whereas this effect was completely rescued
330 by administration of RA.

331 Differential expression testing in the *ZNF503*-KO EBs resulted in a more limited number of
332 differentially expressed genes in either condition (Supplementary Table S2E-F). *LHX2*-KO showed an
333 increase in vCM and aCM markers (Wilcoxon p-adjusted $1.8 \times 10^{-2}$ and $1.2 \times 10^{-8}$, respectively) in the
334 ventricular EB cultures (Fig. 4C, Supplementary Fig. S16 and Table S2C-D). In the atrial cultures, a
335 significant decrease in fibroblast / smooth muscle markers (Wilcoxon p-adjusted $3.1 \times 10^{-3}$) and aCM
336 progenitor markers (Wilcoxon p-adjusted $3.5 \times 10^{-2}$) was observed, to the benefit of the 'other' cluster
337 (Wilcoxon p-adjusted $3.4 \times 10^{-4}$), marking a substantial defect in differentiation in combination with RA
338 treatment.

339 Given this dynamic re-routing of cardiac progenitors along different lineages with these genetic
340 perturbations, we wondered how the observed transcriptomic changes related to both the gene-
341 regulatory networks and the transcription factor motif content in our chromatin accessibility data. We
342 therefore determined the overlap between *ZNF711*-KO differentially expressed genes (DE-genes) and
343 the ZNF711 targets predicted by scANANSE (Methods, Supplementary Table S3). Since scANANSE
344 generates cell type-specific GRNs, we performed this test for the vCM, aCM and epicardial networks.
345 The scANANSE ZNF711 targets were enriched for the ventricular *ZNF711*-KO DE-genes, in both the vCM
346 and aCM networks (fold enrichment 1.4 and 1.9, hypergeometric p-adjusted $5 \times 10^{-05}$ and $2.4 \times 10^{-12}$
347 respectively), but not in the epicardial network, whereas this enrichment was not found for the overlap
348 with the DE-genes in the RA-treated (atrial) condition in any of the cell networks. On a basic level, this
349 confirms the predictive power of the inferred networks. It also suggests that *ZNF711*-KO is directly

350 required for the shared atrial-ventricular CM program, but that RA rescues this program while also
351 conferring an atrial identity to the resulting CMs. Epicardial differentiation occurs in both conditions,
352 but is stimulated by RA in wild type EBs. The upregulation of epicardial markers in the *ZNF711*-KO (Fig.
353 4C) in the absence of RA likely results from rerouting of progenitors to the epicardial lineage at the
354 expense of the blocked CM lineage. Interestingly, performing the same test with the targets predicted
355 by scANANSE for RARB, showed significant enrichment for the ventricular (non-RA) *ZNF711*-KO DE-
356 genes in the target networks of all cell types (Supplementary Table S3). This can explain how RA-
357 treatment rescues CM differentiation in *ZNF711*-KO atrial EB cultures. These analyses also showed
358 significantly enriched overlaps of LHX2 targets in the epicardial and aCM networks and *LHX2*-KO DE
359 genes, and moreover of LHX2 targets and *ZNF711*-KO DE genes and vice versa, but only under RA-
360 treatment conditions (Supplementary Table S3). No major shift is observed in the expression of cell
361 type markers in RA-treated *LHX2*-KO EBs, whereas in the absence of RA, ventricular CM gene expression
362 is stronger and no significant effect is observed for epicardial gene expression (Fig. 4C). This suggests
363 that LHX2 cooperates with RA receptors to activate epicardial and CM gene expression.
364 As summarized in our model (Fig. 4F), the data uncover how the balance of lineage decisions of
365 cardiac progenitors is shifted by genetic perturbations, and is modified in major ways by RA, a natural
366 cardiac crescent morphogen. We find that *ZNF711* is important for the CM program including for the
367 expression of structural sarcomere genes, but only in the absence of RA. The resulting block in CM
368 differentiation redirects progenitors towards the epicardial and endodermal lineages. RA rescues the
369 defect on the general CM program in the absence of ZNF711 and induces the atrial CM identity.
370
371 **Discussion**
372 We present a roadmap of *in vitro* cardiac differentiation, detailing the steps of lineage commitment
373 and differentiation in cardiac monolayer, EB and EHT cultures. This allows for direct comparisons over
374 time and between anterior or posteriorized SHF progenitors. We identified similar multilineage
375 compositions within the atrial and ventricular EB cultures as reported in other cardiac organoid
376 protocols (Meier et al., 2023; Silva et al., 2021). In our experiments, the EBs showcased a plasticity of
377 multipotent progenitor cells that was susceptible to patterning by RA. Because of this high level of
378 plasticity in cardiac cultures and the ability to culture CMs of various specific subtypes (Devalla et al.,
379 2015; Schmidt et al., 2023; Schwach et al., 2017; Zawada et al., 2023), detailed deconstruction of the
380 developmental steps within the culture is necessary, to understand and optimize the cell type
381 composition. The specification of posterior SHF progenitors directed CMs towards an atrial identity, as
382 expected; however, other cell lineages (endothelial, epicardial, fibroblast and SMC-like cells) were
383 minimally affected. Our analysis of the *in vitro* roadmap not only identified known and candidate
384 regulators, but also provides insights when tracing back and interpreting results from knockout studies.

385 Such analysis revealed that *ZNF711* plays a critical role in safe-guarding the ventricular CM lineage,
386 whereas in the absence of both *ZNF711* and RA a major shift towards the epicardial and endodermal
387 lineage is observed.

388 Epicardial and anterior endoderm cell populations have been observed in previous studies
389 (Drakhlis et al., 2021; Hofbauer et al., 2020; Meier et al., 2023; Silva et al., 2021; Zawada et al., 2023).
390 Our findings corroborate these observations and demonstrate that these populations can emerge
391 independently of RA treatment (Drakhlis et al., 2021; Silva et al., 2021). This was confirmed by the
392 expression of markers of the juxta-cardiac field and pre-epicardial cells (Meier et al., 2023), including
393 the expression of the newly identified epicardial markers such as *ITGA8* (Zawada et al., 2023). Paracrine
394 signaling from endodermal and epicardial populations has been reported to be beneficial for both the
395 epicardial and CM cell populations (Quijada et al., 2020). Moreover, anterior endoderm is essential for
396 vertebrate heart development and morphogenesis (Nascone & Mercola, 1995; Withington et al., 2001).
397 As we further characterized our multipotent progenitors around day 8, we identified potential
398 transcriptional regulators that could steer these dynamic cultures to the specific cardiac subtypes. This
399 led to cell type-specific GRNs that represent both known and hitherto unknown regulators of the
400 cardiac development.

401 In our pursuit of candidate regulators, we experimentally identified an important role for *ZNF711*
402 a gene about which comparatively little it known. Mutations in *ZNF711* have been associated with X-
403 linked intellectual disability and an altered DNA methylation signature in blood (Wang et al., 2022).
404 *ZNF711* is a member of a small family of zinc-finger genes that encode a similar N-terminal acidic
405 activation domain (Mardon et al., 1990; Ni et al., 2020). Moreover, ZNF711 can bind CpG island
406 promoters where it can recruit PHF8, a histone H3K9 demethylase (Kleine-Kohlbrecher et al., 2010).
407 Notably, *ZNF711* orthologs are found in the genomes of jawed vertebrates, but not in those of
408 invertebrate animals. Although shared among most bilaterian animals, the heart has evolved
409 significantly in vertebrates, including the addition of chambers and the endocardial and epicardial
410 layers (Carmona et al., 2010; Simões-Costa et al., 2005). The RA pathway was co-opted to derive atrial
411 cardiomyocytes and the epicardial lineage from mesodermal precursors. This may have required
412 changes in the CM specification program to safe-guard the ventricular CM lineage. Our research reveals
413 that *ZNF711* is important for cardiomyocyte differentiation in the absence of RA. In scenarios where
414 both ZNF711 and RA are absent, there is a shift towards the differentiation of epicardial cells at the
415 expense of ventricular cardiomyocytes. Cardiomyocyte commitment is rescued by RA, while
416 simultaneously endowing the cardiomyocytes with an atrial gene expression identity. Consistent with
417 this rescue, we find that regulatory elements of the genes involved contain motifs for both ZNF711 and
418 retinoic acid receptors. Given the plasticity of cardiac mesoderm and heart field progenitors, which are
419 readily redirected to different cell lineages, safe-guards are necessary for balanced lineage

420 differentiation, and ZNF711 appears to have an important role in securing the ventricular
421 cardiomyocyte lineage.
422 The cardiac organoid models and CM differentiation protocols available to date, have been
423 obtained by extensive experimentation and diligent optimization. These models contain different cell
424 types and cell states, reflecting both lineage potential and culture conditions. Further effort will be
425 required to improve these human stem cell-based models by leveraging single-cell roadmaps and gene-
426 regulatory networks generated by us and others. This will increase our fundamental understanding of
427 the heart as a complex tissue, while providing a major impetus for analyses of heart disease
428 mechanisms, heart regeneration and drug screening.
429

430 **DATA AND CODE AVAILABILITY**

431 **Data availability**

432 All NGS data is available on GEO with the temporal scRNA-seq data at GSE263193, the multiome day 8
433 EB samples at GSE263326 and the RNA-seq data of the KO samples at GSE263325. Published data was
434 obtained from GSE106118 (Cui et al., 2019) or as filtered matrices published on the author's website
435 (Asp, 2021; Asp et al., 2019). The single-cell temporal atlas object for visualization can be downloaded
436 through Zenodo via https://doi.org/10.5281/zenodo.10932845. The per-cluster pseudobulk scATAC-
437 seq profiles can be viewed in the Genome Browser at
438 https://genome.ucsc.edu/s/rebecza/scRoadmap_CardiacDiffs_hg38.

439 **Software and script availability**

440 All used software is mentioned in the METHODS, the custom R and Python scripts used for the analyses,
441 as well as instructions on how to visualize the single-cell atlas data in an interactive user interface are
442 available on Github at https://github.com/Rebecza/scRoadmap_CardiacDiffs.

443

444 **ACKNOWLEDGEMENTS**

445 This work was funded by a ZonMw TOP grant (project number 91217061) to R.P. and G.J.C.V.

446

447 **AUTHOR CONTRIBUTIONS**

448 R.R.S. conceived experiments, generated libraries for all Next Generation Sequencing (NGS) methods
449 used in the manuscript, led the computational analysis and wrote the manuscript. C.C.F. conceived
450 experiments, performed all cell culture work used in the manuscript, harvested and sorted the cells,

generated the CRISPR-Cas9 knockout lines and wrote the manuscript. M.B. generated bulk RNA-sequencing libraries and performed the sequencing for all NGS libraries used in the manuscript. V.S. conceived experiments. R.P. conceived experiments, supervised the experiments involving stem cell differentiation, wrote the manuscript and generated funding for the work. G.J.C.V. conceived experiments, supervised computational genomics analysis, wrote the manuscript and generated funding for the work.

**DECLARATION OF INTERESTS**

R.P. is a cofounder of Pluriomics (Ncardia) and River BioMedics BV. The other authors declare no competing interests.

461 **METHODS**

462 **HPSC culture**

463 Experiments were performed using the human embryonic stem cell (hESC) lines NKX2.5$^{EGFP/+}$COUP-
464 TFII$^{mCherry/+}$ (Schwach et al., 2017). hPSCs were maintained as undifferentiated colonies in Essential 8
465 medium (Thermo Fisher, A1517001) on vitronectin (Thermo Fisher, A31804)-coated 6-well plates
466 (Greiner Bio-One, 657160).

467 **Differentiation of hPSCs into ventricular monolayers**

468 Differentiation of hPSCs to VM monolayers was performed as previously described (Birket et al., 2015).
469 Briefly, one day before starting the differentiation, hPSCs were seeded at a density of 20-25x103 cells
470 per $cm^2$ on Matrigel (83 µg protein/mL) (Corning, 354230)-coated 6-well plates in Essential 8 medium.
471 After 24 h (day 0), mesodermal differentiation was induced by addition of Activin-A (20 - 30 ng/mL,
472 Miltenyi 130–115-010), BMP4 (20 -30 ng/mL, R&D systems 314-BP/CF) and WNT activator CHIR99021
473 (1.5 - 2.25 µmol/L, Axon Medchem 1386) in BPEL medium (Ng et al., 2008). At day 3, BPEL containing
474 WNT inhibitor XAV939 (5 µmol/L, R&D Systems 3748) was used to refresh cells. On day 7, 10 and 14
475 cells were refreshed with plain BPEL.

476 **Differentiation of hPSCs into ventricular and atrial EBs**

477 Differentiation of hPSCs to ventricular or atrial EBs was performed as previously described (Schwach et
478 al., 2022). Briefly, hPSC were seeded and aggregated in EB formation medium (Essential 8 containing
479 400 µg/mL Poly (vinil alcohol) (Sigma Aldrich, P8136) and 10 µM Y-27632 (Bio-Connect, S1049)) one
480 day before starting the differentiation. After 24 h (day 0), mesodermal differentiation was induced by
481 addition of Activin-A (30 ng/mL, Miltenyi 130–115-010), BMP4 (30 ng/mL, R&D systems 314-BP/CF),
482 WNT activator CHIR99021 (1.5 µmol/L, Axon Medchem 1386), VEGF (30 ng/µL, Miltenyi Biotec, 130-
483 109-386) and SCF (40ng/µL, Stem Cell Technologies, 78062.1) in BPEL medium (Ng et al., 2008). On day
484 3 of differentiation, EBs were refreshed with plain BPEL. On day 4, atrial EBs were refreshed with either
485 1 µM of all trans RA (Sigma Aldrich, R2625) or 20 µM RARα selective agonist BMS-753 (Torcis
486 Bioscience, 3505). Next day, atrial EBs treated with BMS-753 were refreshed with plain BPEL. EBs at
487 day 7 were plated on 0.1% gelatin coated wells in BPEL medium. EBs were refreshed again with BPEL
488 at day 10. Unless indicated, EBs at day 14 were switched to cardiomyocyte media containing 3',5-
489 Triiodo-L-thyronine sodium salt (T3), Dexamethasone (D) and Long R3 IGF-I human (IGF, I) (CM-TDI)
490 (Birket et al., 2015) and refreshed every 2-3 days until used at day 21.

491 **Generation of engineered heart tissues**

492 Ventricular monolayer, ventricular EBs and atrial EBs were sorted at day 14 to separate CMs positive
493 cells (NKX2.5$^{EGFP/+}$-positive COUP-TFII$^{mCherry/+}$-negative for vCMs and NKX2.5$^{EGFP/+}$-positive COUP-
494 TFII$^{mCherry/+}$-positive for aCMs) and non-CMs (NKX2.5$^{EGFP/+}$-negative). For each CM differentiation
495 (ventricular mono and EBs, and atrial EBs), cells were mixed back at a specific ratio of 80% CMs + 20%
496 non-CMs. EHTs from ventricular monolayers and atrial EBs were generated by following the protocol as
497 described (Ribeiro et al., 2022). As a 2D control, monolayers from each CM differentiation were
498 generated by seeding the cells with the same cell ratio (80% CMs + 20% non-CMs) in vitronectin coated
499 48 wells plates. EHTs and 2D controls were kept in CM-TDI media and refreshed every 2-3 days until
500 use.

501 **Immunohistochemistry and confocal imaging**

502 For whole mount staining on intact EBs, EBs at day 7 were seeded on gelatine-coated glass bottom
503 plates. Cells were fixed at day 21 with 4% Paraformaldehyde for 15 min at RT. Permeabilization was
504 followed with 0.1% Triton X100 for 8 min at RT. After blocking for 1 h at RT with 5% Fetal Bovine Serum
505 (FBS), cells were incubated at 4°C overnight with the primary antibodies (Table 1). After washing, cells
506 were incubated for 1 h at RT with secondary antibodies (Table 1) and 5 min at RT with DAPI. EHTs at
507 day 12 after tissue formation were fixed with 4% Paraformaldehyde for 1 h at RT. Whole tissue
508 immunostaining was performed as described (Ribeiro et al., 2022). Antibodies used are described in
509 Table 1. Confocal images were captured using a Zeiss LSM 880 microscope.

510 **Table 1. Antibodies used for immunohistochemistry on EBs and EHTs**

| Antibody | Cat. Number | Dilution factor |
|---|---|---|
| Rabbit anti-NKX2.5 | Cell Signaling, 8792 | 1:400 |
| Mouse anti-COUP-TFII | Perseus Proteomics, 1:500 | 1:200 |
| Mouse anti-ACTN2 | Sigma, A7811 | 1:800 |
| Rabbit anti-MYL7 | R&D Systems, MAB90961-SP | 1:100 |
| Rabbit anti-MYL2 | Sigma HPA019763 | 1:100 |
| Mouse anti-cTnT | ThermoFisher MA512960 | 1:400 |
| DAPI | Thermo Scientific, D1306 | 1:2000 |

| | | |
|---|---|---|
| Chicken anti Rabbit IgG (H+L) Alexa Fluor 488 | Invitrogen, A-21441 | 1:500 |
| Donkey anti Mouse IgG (H+L) Alexa Fluor 647 | Invitrogen, A-31571 | 1:500 |

511

512 **Optical membrane potential imaging**

513 For optical membrane potential imaging, aCMs or vCMs at day 14 were stained for 30 min at RT with
514 the voltage-sensitive dye FluoVolt™ according to manufacturer. For signal acquisition, the loaded
515 sample was excited using a 488 nm laser and recorded for 10 seconds. Movies were acquired with a
516 Nikon ECLIPSE Ti2 fluorescent microscope under temperature and humidity control (37°C and 5% $CO_2$).
517 Videos were analyzed with BV Workbench, Brainvision Inc.

518 **FACS and flow cytometry**

519 Monolayers and EBs from day 3 to day 8 were dissociated to single cells with TypLE 1X (Thermo Fisher,
520 12563029) for 5 minutes at 37°C. From day 8 onwards, monolayers and EBs were dissociated with TypLE
521 10X (Thermo Fisher, A1217702) for 10 min at 37°C. EHTs were dissociated with collagenase type II
522 (240U/ml) (Worthington Biochemical LS004176) for 20-30 min at 37°C followed by TrypLE 10X for 10-
523 15 min at 37°C. Cells were transferred to FACS buffer (2mM EDTA, 0.5% BSA in DPBS) and filtered (VWR,
524 734-0001). For single cell RNA sequencing, cells were single cell sorted into 384-well primer plates.
525 Sorting was performed with a Sony SH800. Flow cytometry was performed with a MACSQuant Analyzer
526 16 (Miltenyi). Flow cytometry data was analyzed with FlowJo software (Miltenyi).

527 **CEL-Seq2 RNA-sequencing sample preparation**

528 Libraries were prepared in 384-well plate format using a modified SORT-Seq, or CEL-Seq2, protocol
529 (Hashimshony et al., 2016; Muraro et al., 2016). Primer plates were generated with CEL-Seq2
530 compatible oligo's containing the T7 promoter, a 5' Illumina adapter, unique molecular identifiers
531 (UMIs; 8 bp), a unique cell barcode (8 bp) and oligo(dT)N for mRNA molecules tagging. The primers
532 were designed reversed from classic CELSeq2 primers, leading to barcode and UMI priming in read 2,
533 where the transcripts were sequenced from read 1, as previously described (Gerlach et al., 2019). After
534 sorting, the plates were spun down and immediately stored at -80°C and thawed before the reverse
535 transcription PCR (RT-PCR). ERCC RNA Spike-In Mix II (Invitrogen) was added in 1:50 x $10^3$ ratio to each
536 of the wells administered in 150 nL volume by the micro-dispenser Nanodrop II (BioNex). The Nanodrop
537 II was additionally used for dispending the reverse transcription mix, consisting of Superscript II
538 (Invitrogen) and RNasein Plus (Promega), as well as for the second strand synthesis with a mix of E. coli
539 RNase H (Invitrogen), E. coli DNA polymerase and E. coli DNA ligase (New England Biolabs). After the

540 second strand synthesis the cDNA of all single cells of a plate were pooled, before performing an
541 overnight in vitro transcription reaction at 16°C using the MegaScript IVT kit (Invitrogen). Remaining
542 primers were removed by using EXOI/rSAP-IT (Applied Biosystems) and the amplified RNA was
543 chemically fragmented and cleaned up with AMPure XP beads (Beckman Coulter). Using random
544 octamers the following RT was performed, after which the library amplification was one with Phusion
545 High-Fidelity DNA Polymerase (New England Biolabs) during which the Illumina adapters were
546 introduced, as well as the unique index sequence per library (NextFlex DNA barcodes, PerkinElmer).
547 After bead-purification, the library concentration and quality were assessed using the DeNovix and
548 BioAnalyzer High Sensitivity DNA Kit (Agilent Technologies), respectively. Sequencing was performed
549 with the NextSeq 500 (Illumina).

550 **10X Multiome sample preparation**

551 Nuclei from atrial and ventricular EBs at day 8 of differentiation were isolated with an ice-cold lysis
552 buffer consisting of 10 mM Tris-HCl (pH 7.4), 10 mM NaCl, 3 mM MgCl2, 1% BSA, 0.1% Tween-20, 0.1%
553 Nonidet P40 Substitute, 0.01% Digitonin, 1 mM DTT (Invitrogen, cat. no. 18064-014), 1 U/µL Protector
554 RNase inhibitor (Roche, 3335399001) in Nuclease-free water. After three washes with ice-cold
555 nuclease-free water containing 10 mM Tris-HCl (pH 7.4), 10 mM NaCl, 3 mM MgCl2, 1% BSA, 0.1%
556 Tween-20, 1 mM DTT and 1 U/µL RNase inhibitor, isolated nuclei were kept on ice in PBS containing
557 0.04% BSA and 1 mM MgCl2. The amount of nuclei was counted by haematocytometer. Droplet
558 formation and library generation was performed as described using the 10X Genomics Next Gem Single
559 Cell Multiome ATAC + Gene Expression Reagents kit.

560 **Generation of CRISPR-Cas9 knockouts for LHX2, ZNF711 and ZNF503**

561 hPSCs maintained in StemMACS™ PSC-Brew XF (Miltenyi Biotec, 130-127-865) were dissociated as the
562 regular maintenance passaging procedure. Per knock-out target, cell pellets of 200x103 cells were
563 resuspended with 20 µL of supplemented nucleofector solution P3 Primary Cell 4D-Nucleofector® S
564 (Lonza, V4XP3032) with indicated amounts of multi-guide sgRNAs (Synthego) and SpCas9-2NLS
565 Nuclease (Synthego) in a ratio of 3:1, and nucleofected with a 4D-Nucleofector Core and X unit (Lonza)
566 using program CB-150. Human *TRAC* sgRNA was used as a positive control, as recommended by the
567 supplier. After nucleofection, cells were seeded in 2 wells of a vitronectin-coated 24-well plate with
568 StemMACS™ PSC-Brew XF supplemented with 1:200 RevitaCell (Thermo Fisher, A2644501). Cells were
569 kept for 2-3 days. During passaging of each well, cells were expanded and also lysed for PCR
570 amplification and Sanger Sequencing. Two passages after nucleofection, differentiation towards atrial
571 and ventricular lineages was initiated. After atrial and ventricular differentiation, cells were

572 characterized and also lysed for PCR amplification and Sanger sequencing. Knock-out efficiency was
573 evaluated with the ICE CRISPR Analysis tool (Synthego).

574

575 **Bulk RNA-sequencing sample preparation**

576 For the transcription factor knockout validation experiments, RNA was harvested at day 14 of the
577 protocols and purified using the Nucleo Spin RNA (Macherey-Nagel) kit according to the manufacturer's
578 protocol. Libraries were generated with the RiboErase depletion RNA-sequencing protocol by KAPA
579 (Roche, 8098131702) and sequenced on the Illumina Next Seq 2000. Per sample 200 ng of total RNA
580 was used for library preparations with the KAPA RNA HyperPrep Kit with RiboErase (HMR) (Kapa
581 Biosystems), including steps of the oligonucleotide hybridization, rRNA depletion, DNase digestion and
582 RNA elution, were performed as instructed by the manufacturer. Fragmentation and priming were
583 performed at 94°C for 6 min, followed by first-strand synthesis, second strand synthesis and A-tailing,
584 which were performed according to protocol. Library amplification was performed with 10 cycles,
585 followed by a 0.8X bead-based cleanup. Library concentration and quality were assessed using the
586 DeNovix and BioAnalyzer High Sensitivity DNA Kit (Agilent Technologies). Sequencing was performed
587 with the NextSeq 500 (Illumina).

588

589 **COMPUTATIONAL METHODS**

590 **Processing and integration of CEL-Seq2 scRNA-sequencing data**

591 The FASTQs were trimmed and aligned with seq2science v0.4.0 (van der Sande et al., 2023). In short,
592 kb-python v0.25.0 was used for quantifying (kb count with the setting '--technology 1,8,16:1,0,8:0,0,0')
593 to map the reads against the GRCh38 genome and quantify the UMI counts per cell (Melsted et al.,
594 2021). Fluorescence reporter genes and ERCC sequences were added to the genome before the index
595 was generated with kb-python. The combined single-cell gene count matrix was filtered for good
596 quality cells (UMI >= 1,000, detected genes >= 500, mitochondrial genes percentage < 50% or ERCC
597 count < 20%), after which 12706 cells were left for downstream analysis. Scater v1.20.1 was used to
598 perform quality control on the cells of the dataset and check confounding variables within the
599 metadata (McCarthy et al., 2017). Since four culture experiments were combined, the object was split
600 per experiment (Mon, EB or EHT experiment or one experiment combining all three), to individually
601 normalize and select highly variable features (2,000 each) per experiment and finally perform
602 integration anchor selection with Seurat (v4.0.4) (Hao et al., 2021), to lower batch effects and create
603 one larger atlas. Dimensionality reduction was performed with PCA and the first 50 principal

604 components were used to generate the atlas UMAP and compute the shared nearest neighbor graphs
605 using Jaccard index. Louvain clustering was performed with a resolution of 0.9 with the implementation
606 FindClusters in Seurat. Optimal resolution settings for clustering, was evaluated with Clustree v0.4.3
607 (Zappia & Oshlack, 2018). For all gene expression visualizations onto the UMAP, the dots representing
608 cells were plotted in the order of low to high expression.

609 **Atlas integration validation**

610 A total of 33,108 anchors (cell-pairs) were found between the experiments. Anchor pairs from the same
611 time point and method were counted and their scores averaged, which resulted in a per time point and
612 method pairs scoring across the experiments (with a total of 535 of combinations). The product of the
613 mean score and frequency of the anchor (score * (frequency anchor / total number of anchors)) was
614 visualized with the R package pheatmap v1.0.12.

615 **Comparison with in vivo human fetal scRNA-seq data**

616 Two available human fetal scRNA-seq datasets from Cui et al. and Asp et al. were integrated by use of
617 Seurat (Asp et al., 2019; Cui et al., 2019). The annotation of the Asp et al. dataset as established by the
618 authors, was used to annotate the clusters of the integrated dataset. The first 20 principal components
619 were used for running UMAP dimensionality reduction and neighborhood graph, and the Louvain
620 clustering was performed with a resolution of 1. The resulting dataset was used for predicting the cell
621 types of the in vitro atlas clusters, by running the *TransferData* functionality of Seurat on the integrated
622 assays with the in vivo dataset as the reference. The resulting prediction scores per cell of our in vitro
623 atlas (a calculation outlined in the paper of Stuart et al., 2019) were averaged to create a prediction
624 score per atlas cluster and visualized with pheatmap.

625 **RNA velocity on early atlas subsets**

626 Subsets of the atlas were generated by taking the time points of differentiation until day 14 (before
627 transfer to maturation medium) and split per protocol, resulting in three early subsets: ventricular
628 monolayer, atrial and ventricular EB cultures from day 4 to day 14. Dimensionality reduction was
629 performed in Seurat and UMAPs were generated with the first 30 principal components and a minimum
630 distance set to 0.75. The raw spliced, unspliced counts, atlas cluster information and UMAP
631 embeddings from the Seurat object, were transferred to an AnnData object for further analysis with
632 Scanpy v1.8.2 in Python (Wolf et al., 2018). The genes selected for finding the integration anchors were
633 taken along as HVG. RNA velocity was run with scVelo v0.2.4 (Bergen et al., 2020).

634 **Embryoid body differential transcription factor analysis over time**

635 For direct aCM and vCM comparison, a subset of only embryoid body time points was selected.
636 Differential gene expression testing was performed on selected clusters, representing the progenitor
637 stages contributing to aCM and vCM over time. Wilcoxon Rank Sum test was used to find significant
638 differentially expressed genes between the clusters 24 and 6, 14 and 0, 9 and 4 and 2 and 3 (atrial and
639 ventricular clusters, respectively), expressed in at least 25% of the cells in one of the clusters in each
640 comparison and with an adjusted p-value < 0.05. The resulting list of genes was filtered on genes
641 considered to be transcription factors (Lambert et al., 2018). Hierarchical clustering of the factors was
642 performed to separate specific expression patterns over the different time points across the lineages,
643 and the results were visualized using Complex Heatmap v2.8.0 (Gu et al., 2016).

644 **Retinoic acid-related gene sets**

645 Differential expression with Wald's ranking test was performed for each of the time points between the
646 lineages in the EB subset. The significantly upregulated genes in the atrial (the RA-induced condition)
647 over ventricular (non-RA), were separated into three subsets relative to the time of RA administration.
648 This was done in the following way: 1) Early RA genes were genes considered significantly upregulated
649 at day 5, that were not upregulated at d4 or any of the time points after day 5 in aCM over vCM, 2) the
650 Long Term RA genes were selected as not yet upregulated at day 4, but upregulated from day 5 onward
651 and still upregulated at the later time points (d8 and d14) , and 3) the Late RA genes were selected as
652 genes the genes upregulated at d8 and not yet upregulated at day 4 or 5 in aCM over vCM.

653 **Multiome analysis processing and integration**

654 The multiome data was mapped with 10X Genomics Cell Ranger ARC v2.0.1 on the GRCh38 genome.
655 To select droplets containing a quality cell, the cell-calling performed with running Cell Ranger ATAC on
656 the ATAC data alone was combined with setting additional manual thresholds (only keeping droplets
657 with a number of RNA counts > 1,000 and < 10,000, number of ATAC counts > 5,000 and < 20,000,
658 nucleosome signal < 1, TSS enrichment score > 4 and percentage of mitochondrial reads < 20%). The
659 resulting dataset consisted of 17,027 cells and was analyzed using Signac v1.7.0 and Seurat v4.0.3
660 (Stuart et al., 2021). The EB day 8 samples, one from each lineage, were integrated using CCA on the
661 scRNA-seq matrices and visualized using UMAP on the principal components of PCA analysis on the top
662 2,000 highly variable genes of the data. Clustering was also performed on the scRNA-seq matrices.
663 Pearson correlations between the Multiome scRNA-seq clusters and the CEL-Seq2 derived clusters of
664 d8 EB cells, were performed on subsampled (1,000 cells maximum per cluster) datasets, and the R2
665 values per cell-cell comparison was visualized with pheatmap.

666 **Quality control and motif analysis on scATAC-seq pseudobulk of the clusters**

667 Per-cluster pseudobulk BED-files of the scATAC-seq modality of the multiome, were generated using
668 the SplitFragments functionality in Signac. The BED-files were scaled and converted to BedGraph-files
669 using *genomecov* from bedtools v2.30.0 (Quinlan & Hall, 2010), sorted, and processed to BigWig-files
670 using the UCSC *BedGraphToBigWig* function (Kent et al., 2010). Visualization of the BigWig-files was
671 performed in the Genome Browser (Kent et al., 2002), genes without gene name annotation were
672 removed from this view. Peak calling was performed with the MACS2 implementation of Signac, for
673 each of the clusters as well as the pseudobulk of all scATAC-seq reads in the dataset. The subsequent
674 peak summits were merged in case they were at a distance of < 100 bp to one another, and replaced
675 for a summit in the middle of those locations. To generate a merged peak set, all of the summits were
676 extended with 100 bp up- and downstream of the summit. This peak set was used for differentially
677 accessibility testing with the *FindMarkers* functionality from Signac using logistic regression, with the
678 total number of fragments as latent variable. The resulting set was visualized in a bandplot using fluff
679 (REF XX) and used as input for motif scanning analysis using the *maelstrom* function in Gimme Motifs
680 (Bruse & van Heeringen, 2018). Motifs with in at least one of the clusters a z-score > 3, were selected
681 and visualized with its potential binding transcription factors using an adjusted version of the *Motif2TF*
682 function of scANANSE (Smits et al., 2023).

683 **scANANSE analysis on Multiome data**

684 The Seurat implementation of scANANSE (AnanseSeurat, v1.1.0) was used to obtain the important
685 transcription factor regulators from the Multiome dataset (Smits et al., 2023). The resulting differential
686 network for the aCM cluster over vCM cluster, was filtered on the top 20 transcription factors with the
687 highest influence score. Interactions between the nodes with a score > 0.8 were selected from the full
688 cell type-specific networks. Subsequent filtering with the three RA-induced gene sets (described in
689 7.4.18) from the EB analysis, was used to visualize the regulatory hierarchy within the GRN. The GRN
690 visualizations were generated with Cytoscape v3.9.1 (Shannon et al., 2003). The *ZNF711* network was
691 selected from the aCM full network, keeping only interactions with an interaction score > 0.8 and if
692 they were found as factors of influence in this cell type or known cardiac markers.

693 **Validation KOs RNA-seq, lineage marker enrichment and differential analysis**

694 The Seq2Science v0.9.6 pipeline was used to map the RNA-seq reads to the GRCh38 genome (van der
695 Sande et al., 2023). Regularized log transformation was performed with the R package DESeq2 v1.34.0
696 prior to Principal Component Analysis and heatmap visualization of the gene counts (Love et al., 2014).
697 For each of the day 14 EB cell types from the atlas, the top 200 marker genes were selected per cell
698 type lineage. An average expression level per 200 markers was calculated for each of the bulk RNA-seq

samples and corrected for the average expression of the *TRAC* control samples of both conditions, allowing direct comparison between the culture conditions. Significance was tested with a paired Wilcox Sign test for each of the replicates with its matching *TRAC* control sample, which was corrected for multiple testing using the Benjamini & Hochberg method, indicated in the heatmap (p-adjusted < 0.05, < 0.001 and < 0.0001) are based on the highest p-adjusted value per set of replicates. Differential gene expression analysis between *TRAC* control and targeted conditions was performed with DESeq2. The differential gene list was filtered for a log2 fold change > 1 and p-adjusted value < 0.05, and visualized with pheatmap v1.0.12 and EnhancedVolcano v1.12.0. Gene ontology analysis was performed with clusterProfiler v4.2.0 (Wu et al., 2021).

**Hypergeometric test on overlap scANANSE predicted targets and KO targets**

The hypergeometric test was performed with the *phyper* function in R. Per knockout and +RA or non-RA condition, the list of differentially expressed genes was used as *successes* and the overlapping genes between these lists and the scANANSE predicted targets of the *ZNF711*, *LHX2* or *RARB*, were considered the *sample successes* in the hypergeometric tests. All genes (16,232 in total) present in both the mutiome scRNA-seq modality and the bulk RNA-seq samples, were considered the full *population*. The p-values from the hypergeometric tests were corrected for multiple testing using the Benjamini & Hochberg method.

**References**


Ameen, M., Sundaram, L., Banerjee, A., Shen, M., Kundu, S., Nair, S., Shcherbina, A., Gu, M., Wilson, K. D., Varadarajan, A., Vadgama, N., Balsubramani, A., Wu, J. C., Engreitz, J., Farh, K., Karakikes, I., Wang, K. C., Quertermous, T., Greenleaf, W., & Kundaje, A. (2022). Integrative single-cell analysis of cardiogenesis identifies developmental trajectories and non-coding mutations in congenital heart disease. *BioRxiv*, 2022.06.29.498132. https://doi.org/10.1101/2022.06.29.498132

Asp, M. (2021). Developmental heart - filtered and unfiltered count matrices and meta tables. *Mendeley Data*, *Version 2*, Accessed 02-22-2022. https://doi.org/10.17632/MBVHHF8M62.2

Asp, M., Giacomello, S., Fürth, D., Reimegård, J., Wärdell, E., Custodio, J., Salmén, F., Sundström, E., Åkesson, E., Bienko, M., Månsson-Broberg, A., Ståhl, P. L., Sylvén, C., & Lundeberg, J. (2018). An Organ-Wide Gene Expression Atlas of the Developing Human Heart. *SSRN Electronic Journal*. https://doi.org/10.2139/ssrn.3219263

Asp, M., Giacomello, S., Larsson, L., Wu, C., Fürth, D., Qian, X., Wärdell, E., Custodio, J., Reimegård, J., Salmén, F., Österholm, C., Ståhl, P. L., Sundström, E., Åkesson, E., Bergmann, O., Bienko, M., Månsson-Broberg, A., Nilsson, M., Sylvén, C., & Lundeberg, J. (2019). A Spatiotemporal Organ-Wide Gene Expression and Cell Atlas of the Developing Human Heart. *Cell*, *179*(7), 1647-1660.e19. https://doi.org/10.1016/j.cell.2019.11.025

Bergen, V., Lange, M., Peidli, S., Wolf, F. A., & Theis, F. J. (2020). Generalizing RNA velocity to transient cell states through dynamical modeling. *Nature Biotechnology*, *38*(12), 1408–1414. https://doi.org/10.1038/s41587-020-0591-3

Birket, M. J., Ribeiro, M. C., Kosmidis, G., Ward, D., Leitoguinho, A. R., van de Pol, V., Dambrot, C., Devalla, H. D., Davis, R. P., Mastroberardino, P. G., Atsma, D. E., Passier, R., & Mummery, C. L. (2015). Contractile Defect Caused by Mutation in MYBPC3 Revealed under Conditions Optimized for Human PSC-Cardiomyocyte Function. *Cell Reports*, *13*(4), 733–745. https://doi.org/10.1016/j.celrep.2015.09.025

Boobalan, E., Thompson, A. H., Alur, R. P., McGaughey, D. M., Dong, L., Shih, G., Vieta-Ferrer, E. R., Onojafe, I. F., Kalaskar, V. K., Arno, G., Lotery, A. J., Guan, B., Bender, C., Memon, O., Brinster, L., Soleilhavoup, C., Panman, L., Badea, T. C., Minella, A., … Brooks, B. P. (2022). Zfp503/Nlz2 Is Required for RPE Differentiation and Optic Fissure Closure. *Investigative Ophthalmology & Visual Science*, *63*(12). https://doi.org/10.1167/IOVS.63.12.5

Branco, M. A., Dias, T. P., Cabral, J. M. S., Pinto-do-Ó, P., & Diogo, M. M. (2022). Human multilineage pro-epicardium/foregut organoids support the development of an epicardium/myocardium organoid. *Nature Communications 2022 13:1*, *13*(1), 1–18. https://doi.org/10.1038/s41467-022-34730-7

Bruse, N., & van Heeringen, S. J. (2018). GimmeMotifs: An analysis framework for transcription factor motif analysis. *BioRxiv*. https://doi.org/10.1101/474403

Buckingham, M. (2015). First and second heart field. *Congenital Heart Diseases: The Broken Heart: Clinical Features, Human Genetics and Molecular Pathways*, 25–40. https://doi.org/10.1007/978-3-7091-1883-2_3/COVER

Buckingham, M., Meilhac, S., & Zaffran, S. (2005). Building the mammalian heart from two sources of myocardial cells. In *Nature Reviews Genetics* (Vol. 6, Issue 11, pp. 826–835). https://doi.org/10.1038/nrg1710

Burridge, P. W., Keller, G., Gold, J. D., & Wu, J. C. (2012). Production of de novo cardiomyocytes: Human pluripotent stem cell differentiation and direct reprogramming. In *Cell Stem Cell* (Vol. 10, Issue 1, pp. 16–28). https://doi.org/10.1016/j.stem.2011.12.013

Carmona, R., Guadix, J. A., Cano, E., Ruiz-Villalba, A., Portillo-Sánchez, V., Pérez-Pomares, J. M., & Muñoz-Chápuli, R. (2010). The embryonic epicardium: an essential element of cardiac development. *Journal of Cellular and Molecular Medicine*, *14*(8), 2066–2072. https://doi.org/10.1111/J.1582-4934.2010.01088.X

Churko, J. M., Garg, P., Treutlein, B., Venkatasubramanian, M., Wu, H., Lee, J., Wessells, Q. N., Chen, S. Y., Chen, W. Y., Chetal, K., Mantalas, G., Neff, N., Jabart, E., Sharma, A., Nolan, G. P., Salomonis, N., & Wu, J. C. (2018). Defining human cardiac transcription factor hierarchies using integrated single-cell heterogeneity analysis. *Nature Communications*, *9*(1). https://doi.org/10.1038/s41467-018-07333-4

Cui, Y., Zheng, Y., Liu, X., Yan, L., Fan, X., Yong, J., Hu, Y., Dong, J., Li, Q., Wu, X., Gao, S., Li, J., Wen, L., Qiao, J., & Tang, F. (2019). Single-Cell Transcriptome Analysis Maps the Developmental Track of the Human Heart. *Cell Reports*, *26*(7), 1934-1950.e5. https://doi.org/10.1016/j.celrep.2019.01.079

DeLaughter, D. M., Bick, A. G., Wakimoto, H., McKean, D., Gorham, J. M., Kathiriya, I. S., Hinson, J. T., Homsy, J., Gray, J., Pu, W., Bruneau, B. G., Seidman, J. G., & Seidman, C. E. (2016). Single-cell resolution of temporal gene expression during heart development. *Developmental Cell*, *39*(4), 480–490. https://doi.org/10.1016/j.devcel.2016.10.001

Devalla, H. D., & Passier, R. (2018). Cardiac differentiation of pluripotent stem cells and implications for modeling the heart in health and disease. *Science Translational Medicine*, *10*(435). https://doi.org/10.1126/scitranslmed.aah5457

Devalla, H. D., Schwach, V., Ford, J. W., Milnes, J. T., El-Haou, S., Jackson, C., Gkatzis, K., Elliott, D. A., Chuva, S. M., Lopes, S., Mummery, C. L., Verkerk, A. O., & Passier, R. (2015). Atrial-like cardiomyocytes from human pluripotent stem cells are a robust preclinical model for assessing atrial-selective pharmacology. *EMBO Molecular Medicine*, *7*(4), 394–410. https://doi.org/10.15252/EMMM.201404757

Drakhlis, L., Biswanath, S., Farr, C.-M., Lupanow, V., Teske, J., Ritzenhoff, K., Franke, A., Manstein, F., Bolesani, E., Kempf, H., Liebscher, S., Schenke-Layland, K., Hegermann, J., Nolte, L., Meyer, H., de la Roche, J., Thiemann, S., Wahl-Schott, C., Martin, U., & Zweigerdt, R. (2021). Human heart-forming organoids recapitulate early heart and foregut development. *Nature Biotechnology*. https://doi.org/10.1038/s41587-021-00815-9

Farah, E. N., Hu, R. K., Kern, C., Zhang, Q., Lu, T. Y., Ma, Q., Tran, S., Zhang, B., Carlin, D., Monell, A., Blair, A. P., Wang, Z., Eschbach, J., Li, B., Destici, E., Ren, B., Evans, S. M., Chen, S., Zhu, Q., & Chi, N. C. (2024). Spatially organized cellular communities form the developing human heart. *Nature*. https://doi.org/10.1038/S41586-024-07171-Z

Friedman, C. E., Nguyen, Q., Lukowski, S. W., Helfer, A., Chiu, H. S., Miklas, J., Levy, S., Suo, S., Han, J.-D. J., Osteil, P., Peng, G., Jing, N., Baillie, G. J., Senabouth, A., Christ, A. N., Bruxner, T. J., Murry, C. E., Wong, E. S., Ding, J., … Palpant, N. J. (2018). Single-Cell Transcriptomic Analysis of Cardiac Differentiation from Human PSCs Reveals HOPX-Dependent Cardiomyocyte Maturation. *Cell Stem Cell*, *23*(4), 586-598.e8. https://doi.org/10.1016/j.stem.2018.09.009

Fujii, M., Sakaguchi, A., Kamata, R., Nagao, M., Kikuchi, Y., Evans, S. M., Yoshizumi, M., Shimono, A., Saga, Y., & Kokubo, H. (2017). Sfrp5 identifies murine cardiac progenitors for all myocardial structures except for the right ventricle. *Nature Communications 2017 8:1*, *8*(1), 1–9. https://doi.org/10.1038/ncomms14664

Funakoshi, S., Fernandes, I., Mastikhina, O., Wilkinson, D., Tran, T., Dhahri, W., Mazine, A., Yang, D., Burnett, B., Lee, J., Protze, S., Bader, G. D., Nunes, S. S., Laflamme, M., & Keller, G. (2021). Generation of mature compact ventricular cardiomyocytes from human pluripotent stem cells. *Nature Communications 2021 12:1*, *12*(1), 1–23. https://doi.org/10.1038/s41467-021-23329-z

Gaborit, N., Sakuma, R., Wylie, J. N., Kim, K. H., Zhang, S. S., Hui, C. C., & Bruneau, B. G. (2012). Cooperative and antagonistic roles for Irx3 and Irx5 in cardiac morphogenesis and postnatal physiology. *Development (Cambridge, England)*, *139*(21), 4007. https://doi.org/10.1242/DEV.081703

Gerlach, J. P., van Buggenum, J. A. G., Tanis, S. E. J., Hogeweg, M., Heuts, B. M. H., Muraro, M. J., Elze, L., Rivello, F., Rakszewska, A., van Oudenaarden, A., Huck, W. T. S., Stunnenberg, H. G., & Mulder, K. W. (2019). Combined quantification of intracellular (phospho-)proteins and transcriptomics from fixed single cells. *Scientific Reports*, *9*(1). https://doi.org/10.1038/S41598-018-37977-7

Grancharova, T., Gerbin, K. A., Rosenberg, A. B., Roco, C. M., Arakaki, J. E., DeLizo, C. M., Dinh, S. Q., Donovan-Maiye, R. M., Hirano, M., Nelson, A. M., Tang, J., Theriot, J. A., Yan, C., Menon, V., Palecek, S. P., Seelig, G., & Gunawardane, R. N. (2021). A comprehensive analysis of gene expression changes in a high replicate and open-source dataset of differentiating hiPSC-derived cardiomyocytes. *Scientific Reports*, *11*(1), 1–21. https://doi.org/10.1038/s41598-021-94732-1

Gu, Z., Eils, R., & Schlesner, M. (2016). Complex heatmaps reveal patterns and correlations in multidimensional genomic data. *Bioinformatics*.

Guadix, J. A., Orlova, V. V., Giacomelli, E., Bellin, M., Ribeiro, M. C., Mummery, C. L., Pérez-Pomares, J. M., & Passier, R. (2017). Human pluripotent stem cell differentiation into functional epicardial progenitor cells. *Stem Cell Reports*. https://doi.org/10.1016/j.stemcr.2017.10.023

Guo, Y., & Pu, W. T. (2020). Cardiomyocyte maturation: New phase in development. *Circulation Research*, 1086–1106. https://doi.org/10.1161/CIRCRESAHA.119.315862

Haghverdi, L., Lun, A. T. L., Morgan, M. D., & Marioni, J. C. (2018). Batch effects in single-cell RNA-sequencing data are corrected by matching mutual nearest neighbors. *Nature Biotechnology*, *36*(5), 421–427. https://doi.org/10.1038/NBT.4091

Hanawa, M., Takayama, K., Sakurai, F., Tachibana, M., & Mizuguchi, H. (2017). Hepatocyte Nuclear Factor 4 Alpha Promotes Definitive Endoderm Differentiation from Human Induced Pluripotent Stem Cells. *Stem Cell Reviews and Reports*, *13*(4), 542–551. https://doi.org/10.1007/S12015-016-9709-X

Hao, Y., Hao, S., Andersen-Nissen, E., Mauck, W. M., Zheng, S., Butler, A., Lee, M. J., Wilk, A. J., Darby, C., Zager, M., Hoffman, P., Stoeckius, M., Papalexi, E., Mimitou, E. P., Jain, J., Srivastava, A., Stuart, T., Fleming, L. M., Yeung, B., … Satija, R. (2021). Integrated analysis of multimodal single-cell data. *Cell*, *184*(13), 3573-3587.e29. https://doi.org/10.1016/J.CELL.2021.04.048

Hashimshony, T., Senderovich, N., Avital, G., Klochendler, A., de Leeuw, Y., Anavy, L., Gennert, D., Li, S., Livak, K. J., Rozenblatt-Rosen, O., Dor, Y., Regev, A., & Yanai, I. (2016). CEL-Seq2: Sensitive highly-multiplexed single-cell RNA-Seq. *Genome Biology*. https://doi.org/10.1186/s13059-016-0938-8

Hill, M. C., Kadow, Z. A., Li, L., Tran, T. T., Wythe, J. D., & Martin, J. F. (2019). A cellular atlas of Pitx2-dependent cardiac development. *Development (Cambridge)*, *146*(12). https://doi.org/10.1242/DEV.180398/19508

Hofbauer, P., Jahnel, S. M., Papai, N., Giesshammer, M., Deyett, A., Schmidt, C., Penc, M., Tavernini, K., Grdseloff, N., Meledeth, C., Ginistrelli, L. C., Ctortecka, C., Šalic, Š., Novatchkova, M., & Mendjan, S. (2021a). Cardioids reveal self-organizing principles of human cardiogenesis. *Cell*, *184*(12), 3299-3317.e22. https://doi.org/10.1016/J.CELL.2021.04.034/ATTACHMENT/51B85B2F-9A3B-4450-B1FF-520BF80952B4/MMC1.PDF

Hofbauer, P., Jahnel, S. M., Papai, N., Giesshammer, M., Deyett, A., Schmidt, C., Penc, M., Tavernini, K., Grdseloff, N., Meledeth, C., Ginistrelli, L. C., Ctortecka, C., Šalic, Š., Novatchkova, M., & Mendjan, S. (2021b). Cardioids reveal self-organizing principles of human cardiogenesis. *Cell*, *184*(12), 3299-3317.e22. https://doi.org/10.1016/J.CELL.2021.04.034/ATTACHMENT/51B85B2F-9A3B-4450-B1FF-520BF80952B4/MMC1.PDF

Hofbauer, P., Jahnel, S., Papai, N., Giesshammer, M., Tavernini, K., Grdseloff, N., Penc, M., Meledeth, C., Deyett, A., Schmidt, C., Ctortecka, C., Salic, S., Novatchkova, M., & Mendjan, S. (2020). *Cardioids reveal self-organizing principles of human cardiogenesis*. https://doi.org/10.1101/2020.07.06.189431

Itoh, N., Ohta, H., Nakayama, Y., & Konishi, M. (2016). Roles of FGF Signals in Heart Development, Health, and Disease. *Frontiers in Cell and Developmental Biology*, *4*(OCT), 110. https://doi.org/10.3389/FCELL.2016.00110

Kanai-Azuma, M., Kanai, Y., Gad, J. M., Tajima, Y., Taya, C., Kurohmaru, M., Sanai, Y., Yonekawa, H., Yazaki, K., Tam, P. P. L., & Hayashi, Y. (2002). Depletion of definitive gut endoderm in Sox17-null mutant mice. *Development (Cambridge, England)*, *129*(10), 2367–2379. https://doi.org/10.1242/DEV.129.10.2367

Kanki, Y., Kohro, T., Jiang, S., Tsutsumi, S., Mimura, I., Suehiro, J. I., Wada, Y., Ohta, Y., Ihara, S., Iwanari, H., Naito, M., Hamakubo, T., Aburatani, H., Kodama, T., & Minami, T. (2011). Epigenetically coordinated GATA2 binding is necessary for endothelium-specific endomucin expression. *The EMBO Journal*, *30*(13), 2582. https://doi.org/10.1038/EMBOJ.2011.173

Kannan, S., Farid, M., Lin, B. L., Miyamoto, M., & Kwon, C. (2021). Transcriptomic entropy benchmarks stem cell-derived cardiomyocyte maturation against endogenous tissue at single cell level. *PLoS Computational Biology*, *17*(9). https://doi.org/10.1371/JOURNAL.PCBI.1009305

Kent, W. J., Sugnet, C. W., Furey, T. S., Roskin, K. M., Pringle, T. H., Zahler, A. M., & Haussler, and D. (2002). The human genome browser at UCSC. *Genome Research*, *12*(6), 996–1006. https://doi.org/10.1101/GR.229102

Kent, W. J., Zweig, A. S., Barber, G., Hinrichs, A. S., & Karolchik, D. (2010). BigWig and BigBed: enabling browsing of large distributed datasets. *Bioinformatics (Oxford, England)*, *26*(17), 2204–2207. https://doi.org/10.1093/BIOINFORMATICS/BTQ351

Kim, K. H., Rosen, A., Hussein, S. M. I., Puviindran, V., Korogyi, A. S., Chiarello, C., Nagy, A., Hui, C. C., & Backx, P. H. (2016). Irx3 is required for postnatal maturation of the mouse ventricular conduction system. *Scientific Reports 2016 6:1*, *6*(1), 1–14. https://doi.org/10.1038/srep19197

Kleine-Kohlbrecher, D., Christensen, J., Vandamme, J., Abarrategui, I., Bak, M., Tommerup, N., Shi, X., Gozani, O., Rappsilber, J., Salcini, A. E., & Helin, K. (2010). A Functional Link between the Histone Demethylase PHF8 and the Transcription Factor ZNF711 in X-Linked Mental Retardation. *Molecular Cell*, *38*(2–2), 165. https://doi.org/10.1016/J.MOLCEL.2010.03.002

Lambert, S. A., Jolma, A., Campitelli, L. F., Das, P. K., Yin, Y., Albu, M., Chen, X., Taipale, J., Hughes, T. R., & Weirauch, M. T. (2018). The Human Transcription Factors. *Cell*, *172*(4), 650–665. https://doi.org/10.1016/J.CELL.2018.01.029

Lee, J. H., Protze, S. I., Laksman, Z., Backx, P. H., & Keller, G. M. (2017). Human Pluripotent Stem Cell-Derived Atrial and Ventricular Cardiomyocytes Develop from Distinct Mesoderm Populations. *Cell Stem Cell*, *21*(2), 179-194.e4. https://doi.org/10.1016/J.STEM.2017.07.003

Lescroart, F., Chabab, S., Lin, X., Rulands, S., Paulissen, C., Rodolosse, A., Auer, H., Achouri, Y., Dubois, C., Bondue, A., Simons, B. D., & Blanpain, C. (2014). Early lineage restriction in temporally distinct populations of Mesp1 progenitors during mammalian heart development. *Nature Cell Biology*, *16*(9), 829–840. https://doi.org/10.1038/ncb3024

Lescroart, F., Wang, X., Lin, X., Swedlund, B., Gargouri, S., Sànchez-Dànes, A., Moignard, V., Dubois, C., Paulissen, C., Kinston, S., Göttgens, B., & Blanpain, C. (2018). Defining the earliest step of cardiovascular lineage segregation by single-cell RNA-seq. *Science*, *359*(6380), 1177–1181. https://doi.org/10.1126/science.aao4174

Lescroart, F., & Zaffran, S. (2018). Hox and Tale transcription factors in heart development and disease. *The International Journal of Developmental Biology*, *62*(11–12), 837–846. https://doi.org/10.1387/ijdb.180192sz

Lescroart, F., & Zaffran, S. (2022). Single Cell Approaches to Understand the Earliest Steps in Heart Development. *Current Cardiology Reports*, *24*(6). https://doi.org/10.1007/S11886-022-01681-W

Lewis-Israeli, Y. R., Wasserman, A. H., Gabalski, M. A., Volmert, B. D., Ming, Y., Ball, K. A., Yang, W., Zou, J., Ni, G., Pajares, N., Chatzistavrou, X., Li, W., Zhou, C., & Aguirre, A. (2021). Self-assembling human heart organoids for the modeling of cardiac development and congenital heart disease. *Nature Communications 2021 12:1*, *12*(1), 1–16. https://doi.org/10.1038/s41467-021-25329-5

Love, M. I., Huber, W., & Anders, S. (2014). Moderated estimation of fold change and dispersion for RNA-seq data with DESeq2. *Genome Biology*, *15*(12), 1–21. https://doi.org/10.1186/S13059-014-0550-8/FIGURES/9

Mardon, G., Luoh, S.-W., Simpson, E. M., Gill, G., Brown, L. G., & Page, D. C. (1990). Mouse Zfx

917 protein is similar to Zfy-2: each contains an acidic activating domain and 13 zinc fingers.
918 *Molecular and Cellular Biology*, *10*(2), 681–688. https://doi.org/10.1128/MCB.10.2.681-
919 688.1990

920 Marques, I. J., Ernst, A., Arora, P., Vianin, A., Hetke, T., Sanz-Morejón, A., Naumann, U., Odriozola, A.,
921 Langa, X., Andrés-Delgado, L., Zuber, B., Torroja, C., Osterwalder, M., Simões, F. C., Englert, C., &
922 Mercader, N. (2022). Wt1 transcription factor impairs cardiomyocyte specification and drives a
923 phenotypic switch from myocardium to epicardium. *Development (Cambridge, England)*,
924 *149*(6). https://doi.org/10.1242/DEV.200375

925 McCarthy, D. J., Campbell, K. R., Lun, A. T. L., & Wills, Q. F. (2017). Scater: pre-processing, quality
926 control, normalization and visualization of single-cell RNA-seq data in R. *Bioinformatics*, *33*(8),
927 btw777. https://doi.org/10.1093/bioinformatics/btw777

928 Meier, A. B., Zawada, D., De Angelis, M. T., Martens, L. D., Santamaria, G., Zengerle, S., Nowak-
929 Imialek, M., Kornherr, J., Zhang, F., Tian, Q., Wolf, C. M., Kupatt, C., Sahara, M., Lipp, P., Theis, F.
930 J., Gagneur, J., Goedel, A., Laugwitz, K. L., Dorn, T., & Moretti, A. (2023). Epicardioid single-cell
931 genomics uncovers principles of human epicardium biology in heart development and disease.
932 *Nature Biotechnology 2023*, 1–14. https://doi.org/10.1038/s41587-023-01718-7

933 Meilhac, S. M., & Buckingham, M. E. (2018). The deployment of cell lineages that form the
934 mammalian heart. *Nature Reviews Cardiology*, *15*(11), 705–724.
935 https://doi.org/10.1038/s41569-018-0086-9

936 Melsted, P., Booeshaghi, A. S., Liu, L., Gao, F., Lu, L., Min, K. H. (Joseph), da Veiga Beltrame, E.,
937 Hjörleifsson, K. E., Gehring, J., & Pachter, L. (2021). Modular, efficient and constant-memory
938 single-cell RNA-seq preprocessing. *Nature Biotechnology*, *39*(7), 813–818.
939 https://doi.org/10.1038/s41587-021-00870-2

940 Mononen, M. M., Yan Leung, C., Xu, J., Chien, K. R., & Kenneth Chien, C. R. (2020). Trajectory
941 mapping of human embryonic stem cell cardiogenesis reveals lineage branch points and an ISL1
942 progenitor-derived cardiac fibroblast lineage. *Stem Cells*, *38*(10), 1267–1278.
943 https://doi.org/10.1002/stem.3236

944 Mummery, C. L., Zhang, J., Ng, E. S., Elliott, D. A., Elefanty, A. G., & Kamp, T. J. (2012). Differentiation
945 of Human ES and iPS Cells to Cardiomyocytes: A Methods Overview. *Circulation Research*,
946 *111*(3), 344. https://doi.org/10.1161/CIRCRESAHA.110.227512

947 Muraro, M. J., Dharmadhikari, G., Grün, D., Groen, N., Dielen, T., Jansen, E., van Gurp, L., Engelse, M.
948 A., Carlotti, F., de Koning, E. J. P., & van Oudenaarden, A. (2016). A Single-Cell Transcriptome
949 Atlas of the Human Pancreas. *Cell Systems*, *3*(4), 385-394.e3.
950 https://doi.org/10.1016/j.cels.2016.09.002

951 Nakamura, M., Choe, S. K., Runko, A. P., Gardner, P. D., & Sagerström, C. G. (2008). Nlz1/Znf703 acts
952 as a repressor of transcription. *BMC Developmental Biology*, *8*(1), 1–12.
953 https://doi.org/10.1186/1471-213X-8-108/FIGURES/6

954 Nascone, N., & Mercola, M. (1995). An inductive role for the endoderm in Xenopus cardiogenesis.
955 *Development (Cambridge, England)*, *121*(2), 515–523. https://doi.org/10.1242/DEV.121.2.515

956 Ng, E. S., Davis, R., Stanley, E. G., & Elefanty, A. G. (2008). A protocol describing the use of a
957 recombinant protein-based, animal product-free medium (APEL) for human embryonic stem
958 cell differentiation as spin embryoid bodies. *Nature Protocols*, *3*(5), 768–776.
959 https://doi.org/10.1038/nprot.2008.42

960 Ni, W., Perez, A. A., Schreiner, S., Nicolet, C. M., & Farnham, P. J. (2020). Characterization of the ZFX

family of transcription factors that bind downstream of the start site of CpG island promoters. *Nucleic Acids Research*, *48*(11), 5986. https://doi.org/10.1093/NAR/GKAA384

Pezhouman, A., Nguyen, N. B., Sercel, A. J., Nguyen, T. L., Daraei, A., Sabri, S., Chapski, D. J., Zheng, M., Patananan, A. N., Ernst, J., Plath, K., Vondriska, T. M., Teitell, M. A., & Ardehali, R. (2021). Transcriptional, Electrophysiological, and Metabolic Characterizations of hESC-Derived First and Second Heart Fields Demonstrate a Potential Role of TBX5 in Cardiomyocyte Maturation. *Frontiers in Cell and Developmental Biology*, *9*. https://doi.org/10.3389/FCELL.2021.787684

Protze, S. I., Lee, J. H., & Keller, G. M. (2019). Human Pluripotent Stem Cell-Derived Cardiovascular Cells: From Developmental Biology to Therapeutic Applications. *Cell Stem Cell*, *25*(3), 311–327. https://doi.org/10.1016/J.STEM.2019.07.010

Quaranta, R., Fell, J., Rühle, F., Rao, J., Piccini, I., Araúzo-Bravo, M. J., Verkerk, A. O., Stoll, M., & Greber, B. (2018). Revised roles of ISL1 in a hES cell-based model of human heart chamber specification. *ELife*, *7*. https://doi.org/10.7554/ELIFE.31706

Quijada, P., Trembley, M. A., & Small, E. M. (2020). The Role of the Epicardium during Heart Development and Repair. *Circulation Research*, 377–394. https://doi.org/10.1161/CIRCRESAHA.119.315857

Quinlan, A. R., & Hall, I. M. (2010). BEDTools: a flexible suite of utilities for comparing genomic features. *Bioinformatics (Oxford, England)*, *26*(6), 841–842. https://doi.org/10.1093/BIOINFORMATICS/BTQ033

Rana, M. S., Théveniau-Ruissy, M., De Bono, C., Mesbah, K., Francou, A., Rammah, M., Domínguez, J. N., Roux, M., Laforest, B., Anderson, R. H., Mohun, T., Zaffran, S., Christoffels, V. M., & Kelly, R. G. (2014). Tbx1 coordinates addition of posterior second heart field progenitor cells to the arterial and venous poles of the heart. *Circulation Research*, *115*(9), 790–799. https://doi.org/10.1161/CIRCRESAHA.115.305020

Ribeiro, M. C., Rivera-Arbeláez, J. M., Cofiño-Fabres, C., Schwach, V., Slaats, R. H., Ten Den, S. A., Vermeul, K., van den Berg, A., Pérez-Pomares, J. M., Segerink, L. I., Guadix, J. A., & Passier, R. (2022). A New Versatile Platform for Assessment of Improved Cardiac Performance in Human-Engineered Heart Tissues. *Journal of Personalized Medicine*, *12*(2), 12. https://doi.org/10.3390/JPM12020214/S1

Roux, M., Zaffran, S., Zappavigna, V., & Conway, S. J. (2016). Hox Genes in Cardiovascular Development and Diseases. *Journal of Developmental Biology*, *4*(2). https://doi.org/10.3390/JDB4020014

Ruan, H., Liao, Y., Ren, Z., Mao, L., Yao, F., Yu, P., Ye, Y., Zhang, Z., Li, S., Xu, H., Liu, J., Diao, L., Zhou, B., Han, L., & Wang, L. (2019). Single-cell reconstruction of differentiation trajectory reveals a critical role of ETS1 in human cardiac lineage commitment. *BMC Biology*, *17*(1), 1–16. https://doi.org/10.1186/S12915-019-0709-6/FIGURES/6

Saga, Y., Miyagawa-Tomita, S., Takagi, A., Kitajima, S., Miyazaki, J. I., & Inoue, T. (1999). MesP1 is expressed in the heart precursor cells and required for the formation of a single heart tube. *Development*, *126*(15), 3437–3447. https://doi.org/10.1242/DEV.126.15.3437

Sahara, M., Santoro, F., Sohlmér, J., Zhou, C., Witman, N., Leung, C. Y., Mononen, M., Bylund, K., Gruber, P., & Chien, K. R. (2019). Population and Single-Cell Analysis of Human Cardiogenesis Reveals Unique LGR5 Ventricular Progenitors in Embryonic Outflow Tract. *Developmental Cell*, *48*(4), 475-490.e7. https://doi.org/10.1016/j.devcel.2019.01.005

Schmidt, C., Deyett, A., Ilmer, T., Haendeler, S., Torres Caballero, A., Novatchkova, M., Netzer, M. A.,

Ceci Ginistrelli, L., Mancheno Juncosa, E., Bhattacharya, T., Mujadzic, A., Pimpale, L., Jahnel, S. M., Cirigliano, M., Reumann, D., Tavernini, K., Papai, N., Hering, S., Hofbauer, P., & Mendjan, S. (2023). Multi-chamber cardioids unravel human heart development and cardiac defects. *Cell*, *186*(25), 5587-5605.e27. https://doi.org/10.1016/j.cell.2023.10.030

Schwach, V., Cofiño-Fabres, C., Ten Den, S. A., & Passier, R. (2022). Improved Atrial Differentiation of Human Pluripotent Stem Cells by Activation of Retinoic Acid Receptor Alpha (RARα). *Journal of Personalized Medicine*, *12*(4). https://doi.org/10.3390/JPM12040628

Schwach, V., Verkerk, A. O., Mol, M., Monshouwer-Kloots, J. J., Devalla, H. D., Orlova, V. V., Anastassiadis, K., Mummery, C. L., Davis, R. P., & Passier, R. (2017). A COUP-TFII Human Embryonic Stem Cell Reporter Line to Identify and Select Atrial Cardiomyocytes. *Stem Cell Reports*. https://doi.org/10.1016/j.stemcr.2017.10.024

Séguin, C. A., Draper, J. S., Nagy, A., & Rossant, J. (2008). Establishment of endoderm progenitors by SOX transcription factor expression in human embryonic stem cells. *Cell Stem Cell*, *3*(2), 182–195. https://doi.org/10.1016/J.STEM.2008.06.018

Sendra, M., Domínguez, J. N., Torres, M., & Ocaña, O. H. (2021). Dissecting the Complexity of Early Heart Progenitor Cells. *Journal of Cardiovascular Development and Disease 2022, Vol. 9, Page 5*, *9*(1), 5. https://doi.org/10.3390/JCDD9010005

Shahi, P., Wang, C. Y., Lawson, D. A., Slorach, E. M., Lu, A., Yu, Y., Lai, M. D., Velozo, H. G., & Werb, Z. (2017). ZNF50 3/ Zpo2 drives aggressive breast cancer progression by down-regulation of GATA3 expression. *Proceedings of the National Academy of Sciences of the United States of America*, *114*(12), 3169–3174. https://doi.org/10.1073/PNAS.1701690114

Shannon, P., Markiel, A., Ozier, O., Baliga, N. S., Wang, J. T., Ramage, D., Amin, N., Schwikowski, B., & Ideker, T. (2003). Cytoscape: a software environment for integrated models of biomolecular interaction networks. *Genome Research*, *13*(11), 2498–2504.

Silva, A. C., Matthys, O. B., Joy, D. A., Kauss, M. A., Natarajan, V., Lai, M. H., Turaga, D., Blair, A. P., Alexanian, M., Bruneau, B. G., & McDevitt, T. C. (2021). Co-emergence of cardiac and gut tissues promotes cardiomyocyte maturation within human iPSC-derived organoids. *Stem Cell*, *28*, 2137-2152.e6. https://doi.org/10.1016/j.stem.2021.11.007

Simões-Costa, M. S., Vasconcelos, M., Sampaio, A. C., Cravo, R. M., Linhares, V. L., Hochgreb, T., Yan, C. Y. I., Davidson, B., & Xavier-Neto, J. (2005). The evolutionary origin of cardiac chambers. *Developmental Biology*, *277*(1), 1–15. https://doi.org/10.1016/J.YDBIO.2004.09.026

Smits, J. G. A., Arts, J. A., Frölich, S., Snabel, R. R., Heuts, B. M. H., Martens, J. H. A., van Heeringen, S. J., & Zhou, H. (2023). scANANSE gene regulatory network and motif analysis of single-cell clusters. *F1000Research 2023 12:243*, *12*, 243. https://doi.org/10.12688/f1000research.130530.1

Steimle, J. D., & Moskowitz, I. P. (2017). TBX5: A Key Regulator of Heart Development. *Current Topics in Developmental Biology*, *122*, 195. https://doi.org/10.1016/BS.CTDB.2016.08.008

Stuart, T., Butler, A., Hoffman, P., Hafemeister, C., Papalexi, E., Mauck, W. M., Hao, Y., Stoeckius, M., Smibert, P., & Satija, R. (2019). Comprehensive Integration of Single-Cell Data. *Cell*, *177*(7), 1888-1902.e21. https://doi.org/10.1016/j.cell.2019.05.031

Stuart, T., Srivastava, A., Madad, S., Lareau, C. A., & Satija, R. (2021). Single-cell chromatin state analysis with Signac. *Nature Methods 2021 18:11*, *18*(11), 1333–1341. https://doi.org/10.1038/s41592-021-01282-5

Sweat, M. E., Cao, Y., Zhang, X., Burnicka-Turek, O., Perez-Cervantes, C., Akerberg, B. N., Ma, Q.,

Wakimoto, H., Gorham, J. M., Song, M. K., Trembley, M. A., Wang, P., Lu, F., Gianeselli, M., Prondzynski, M., Bortolin, R. H., Seidman, J. G., Seidman, C. E., Moskowitz, I. P., & Pu, W. T. (2023). Tbx5 maintains atrial identity by regulating an atrial enhancer network. *BioRxiv : The Preprint Server for Biology*. https://doi.org/10.1101/2023.04.21.537535

Takahashi, K., Tanabe, K., Ohnuki, M., Narita, M., Ichisaka, T., Tomoda, K., & Yamanaka, S. (2007). Induction of Pluripotent Stem Cells from Adult Human Fibroblasts by Defined Factors. *Cell*, *131*(5), 861–872. https://doi.org/10.1016/j.cell.2007.11.019

Thomson, J. A., Itskovitz-Eldor, J., Shapiro, S. S., Waknitz, M. A., Swiergiel, J. J., Marshall, V. S., & Jones, J. M. (1998). Embryonic stem cell lines derived from human blastocysts. *Science*, *282*(5391), 1145–1147. https://doi.org/10.1126/SCIENCE.282.5391.1145

Tyser, R. C. V. (2023). Formation of the Heart: Defining Cardiomyocyte Progenitors at Single-Cell Resolution. *Current Cardiology Reports*, *1*, 1–9. https://doi.org/10.1007/S11886-023-01880-Z/TABLES/1

Tyser, R. C. V., Mahammadov, E., Nakanoh, S., Vallier, L., Scialdone, A., & Srinivas, S. (2021). Single-cell transcriptomic characterization of a gastrulating human embryo. *Nature 2021 600:7888*, *600*(7888), 285–289. https://doi.org/10.1038/s41586-021-04158-y

van der Sande, M., Frölich, S., Schäfers, T., Smits, J. G. A., Snabel, R. R., Rinzema, S., & van Heeringen, S. J. (2023). Seq2science: an end-to-end workflow for functional genomics analysis. *PeerJ*, *11*. https://doi.org/10.7717/PEERJ.16380

von Gise, A., Zhou, B., Honor, L. B., Ma, Q., Petryk, A., & Pu, W. T. (2011). WT1 regulates epicardial epithelial to mesenchymal transition through β-catenin and retinoic acid signaling pathways. *Developmental Biology*, *356*(2), 421–431. https://doi.org/10.1016/J.YDBIO.2011.05.668

Wang, J., Foroutan, A., Richardson, E., Skinner, S. A., Reilly, J., Kerkhof, J., Curry, C. J., Tarpey, P. S., Robertson, S. P., Maystadt, I., Keren, B., Dixon, J. W., Skinner, C., Stapleton, R., Ruaud, L., Gumus, E., Lakeman, P., Alders, M., Tedder, M. L., … Stevenson, R. E. (2022). Clinical findings and a DNA methylation signature in kindreds with alterations in ZNF711. *European Journal of Human Genetics : EJHG*, *30*(4), 420–427. https://doi.org/10.1038/S41431-021-01018-1

Wiesinger, A., Li, J., Fokkert, L., Bakker, P., Verkerk, A. O., Christoffels, V. M., Boink, G. J. J., & Devalla, H. D. (2022). A single cell transcriptional roadmap of human pacemaker cell differentiation. *ELife*, *11*. https://doi.org/10.7554/ELIFE.76781

Withington, S., Beddington, R., & Cooke, J. (2001). Foregut endoderm is required at head process stages for anteriormost neural patterning in chick. *Development (Cambridge, England)*, *128*(3), 309–320. https://doi.org/10.1242/DEV.128.3.309

Wolf, F. A., Angerer, P., & Theis, F. J. (2018). SCANPY: Large-scale single-cell gene expression data analysis. *Genome Biology*, *19*(1), 1–5. https://doi.org/10.1186/S13059-017-1382-0/FIGURES/1

Wu, T., Hu, E., Xu, S., Chen, M., Guo, P., Dai, Z., Feng, T., Zhou, L., Tang, W., Zhan, L., Fu, X., Liu, S., Bo, X., & Yu, G. (2021). clusterProfiler 4.0: A universal enrichment tool for interpreting omics data. *Innovation (Cambridge (Mass.))*, *2*(3). https://doi.org/10.1016/J.XINN.2021.100141

Xin, M., Davis, C. A., Molkentin, J. D., Lien, C. L., Duncan, S. A., Richardson, J. A., & Olson, E. N. (2006). A threshold of GATA4 and GATA6 expression is required for cardiovascular development. *Proceedings of the National Academy of Sciences of the United States of America*, *103*(30), 11189–11194. https://doi.org/10.1073/PNAS.0604604103/SUPPL_FILE/04604FIG6.PDF

Xu, Q., Georgiou, G., Frölich, S., Van Der Sande, M., Veenstra, G. J. C., Zhou, H., & Van Heeringen, S. J. (2021). ANANSE: an enhancer network-based computational approach for predicting key

transcription factors in cell fate determination. *Nucleic Acids Research*, *49*(14), 7966–7985. https://doi.org/10.1093/NAR/GKAB598

Yang, D., Gomez-Garcia, J., Funakoshi, S., Tran, T., Fernandes, I., Bader, G. D., Laflamme, M. A., & Keller, G. M. (2022). Modeling human multi-lineage heart field development with pluripotent stem cells. *Cell Stem Cell*, *29*(9), 1382-1401.e8. https://doi.org/10.1016/J.STEM.2022.08.007

Yu, J., Vodyanik, M. A., Smuga-Otto, K., Antosiewicz-Bourget, J., Frane, J. L., Tian, S., Nie, J., Jonsdottir, G. A., Ruotti, V., Stewart, R., Slukvin, I. I., & Thomson, J. A. (2007). Induced pluripotent stem cell lines derived from human somatic cells. *Science (New York, N.Y.)*, *318*(5858), 1917–1920. https://doi.org/10.1126/SCIENCE.1151526

Zappia, L., & Oshlack, A. (2018). Clustering trees: a visualization for evaluating clusterings at multiple resolutions. *GigaScience*, *7*(7), 1–9. https://doi.org/10.1093/GIGASCIENCE/GIY083

Zawada, D., Kornherr, J., Meier, A. B., Santamaria, G., Dorn, T., Nowak-Imialek, M., Ortmann, D., Zhang, F., Lachmann, M., Dreßen, M., Ortiz, M., Mascetti, V. L., Harmer, S. C., Nobles, M., Tinker, A., De Angelis, M. T., Pedersen, R. A., Grote, P., Laugwitz, K. L., … Goedel, A. (2023). Retinoic acid signaling modulation guides in vitro specification of human heart field-specific progenitor pools. *Nature Communications 2023 14:1*, *14*(1), 1–20. https://doi.org/10.1038/s41467-023-36764-x

Zeng, B., Liu, Z., Lu, Y., Zhong, S., Qin, S., Huang, L., Zeng, Y., Li, Z., Dong, H., Shi, Y., Yang, J., Dai, Y., Ma, Q., Sun, L., Bian, L., Han, D., Chen, Y., Qiu, X., Wang, W., … Wang, X. (2023). The single-cell and spatial transcriptional landscape of human gastrulation and early brain development. *Cell Stem Cell*, *30*(6), 851-866.e7. https://doi.org/10.1016/J.STEM.2023.04.016

Zhang, Q., Jiang, J., Han, P., Yuan, Q., Zhang, J., Zhang, X., Xu, Y., Cao, H., Meng, Q., Chen, L., Tian, T., Wang, X., Li, P., Hescheler, J., Ji, G., & Ma, Y. (2010). Direct differentiation of atrial and ventricular myocytes from human embryonic stem cells by alternating retinoid signals. *Cell Research 2011 21:4*, *21*(4), 579–587. https://doi.org/10.1038/cr.2010.163

## FIGURES

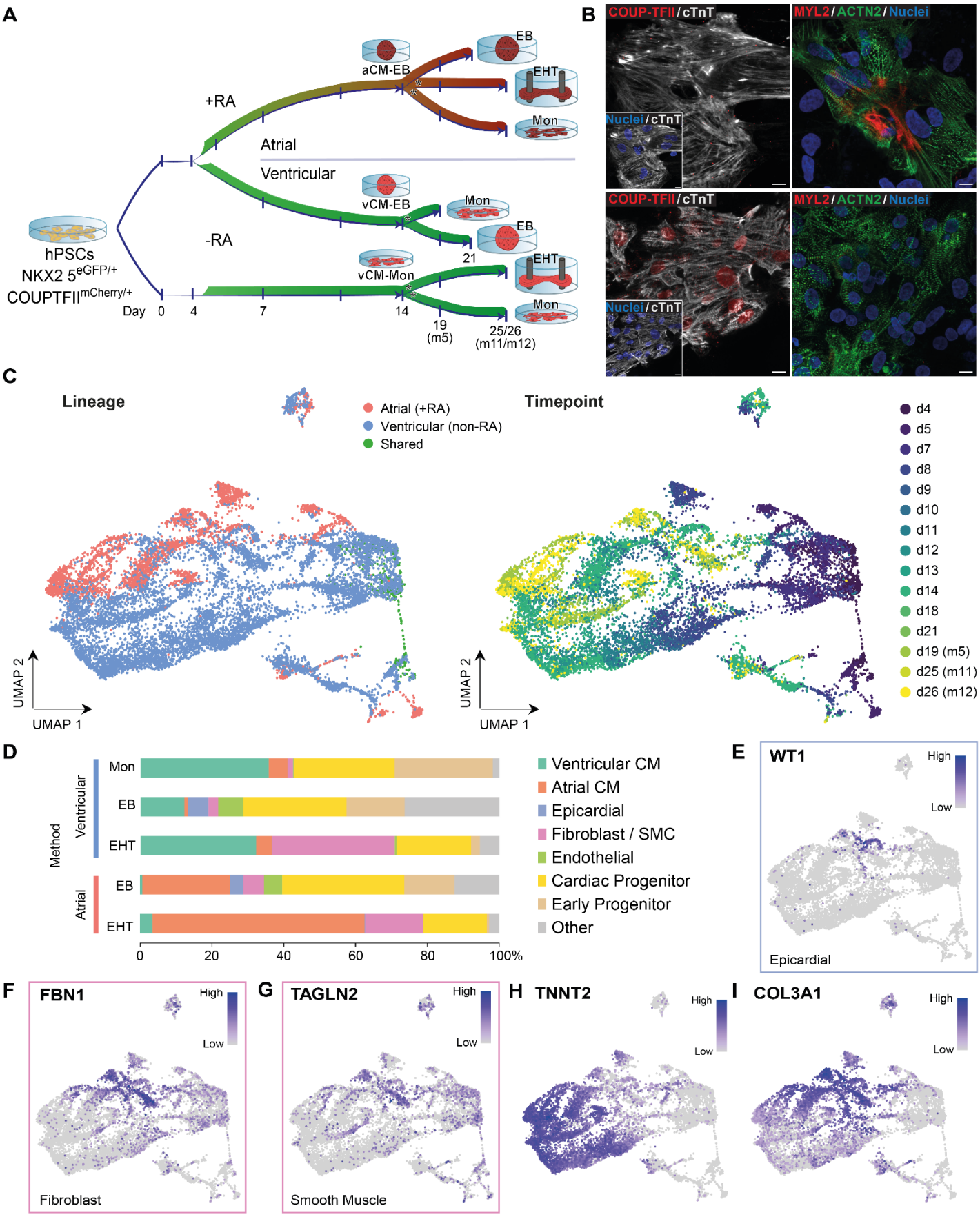


**Figure 1. Confirming cardiac cell types *in vitro* with *in vivo* comparison.**

(A) Human pluripotent stem cell (hPSC)-derived cardiomyocyte differentiation cultures set up. hPSCs are differentiated in monolayer (Mon) or embryoid body (EB) cultures over the course of 14. At day 14 sorted CMs and non-CMs are replated in engineered heart tissues (EHT) to further mature, or replated as monolayers for comparison of the 3D culture (indicated with stars), while the EBs are kept in culture until day 21 (detailed overview of differentiation

protocols in Supplementary Fig. S1). RA = retinoic acid, CM = cardiomyocyte, Mon = monolayer, EB = embryoid body, EHT = engineered heart tissue. d1-21 = day 1-21, m5-m12 = day 5-12 in maturation medium (day 14-26; EHT and monolayer only).

(B) Immunohistochemistry of atrial (COUP-TFII / NR2F2), ventricular (MYL2) and general cardiomyocyte (cTnT / TNNT2 and ACTN2) marker genes in day 14 cardiomyocytes of both the vCM (top row) and aCM (retinoic acid treated; bottom row) culture conditions. Scale bar = 10 (COUP-TFII/cTnT) and 20 µm.

(C) Single-cell temporal atlas UMAP labelled with culture conditions (left) and time point of harvest (right).

(D) Proportions of the different cell states per culture method. Cell states annotation process is shown in Fig. S4.

(E-G) Cell type marker expression levels visualized onto the atlas UMAP.

(H-I) Inversely related expression patterns of TNNT2 (H) and COL3A1 (I) visualized onto the atlas UMAP.

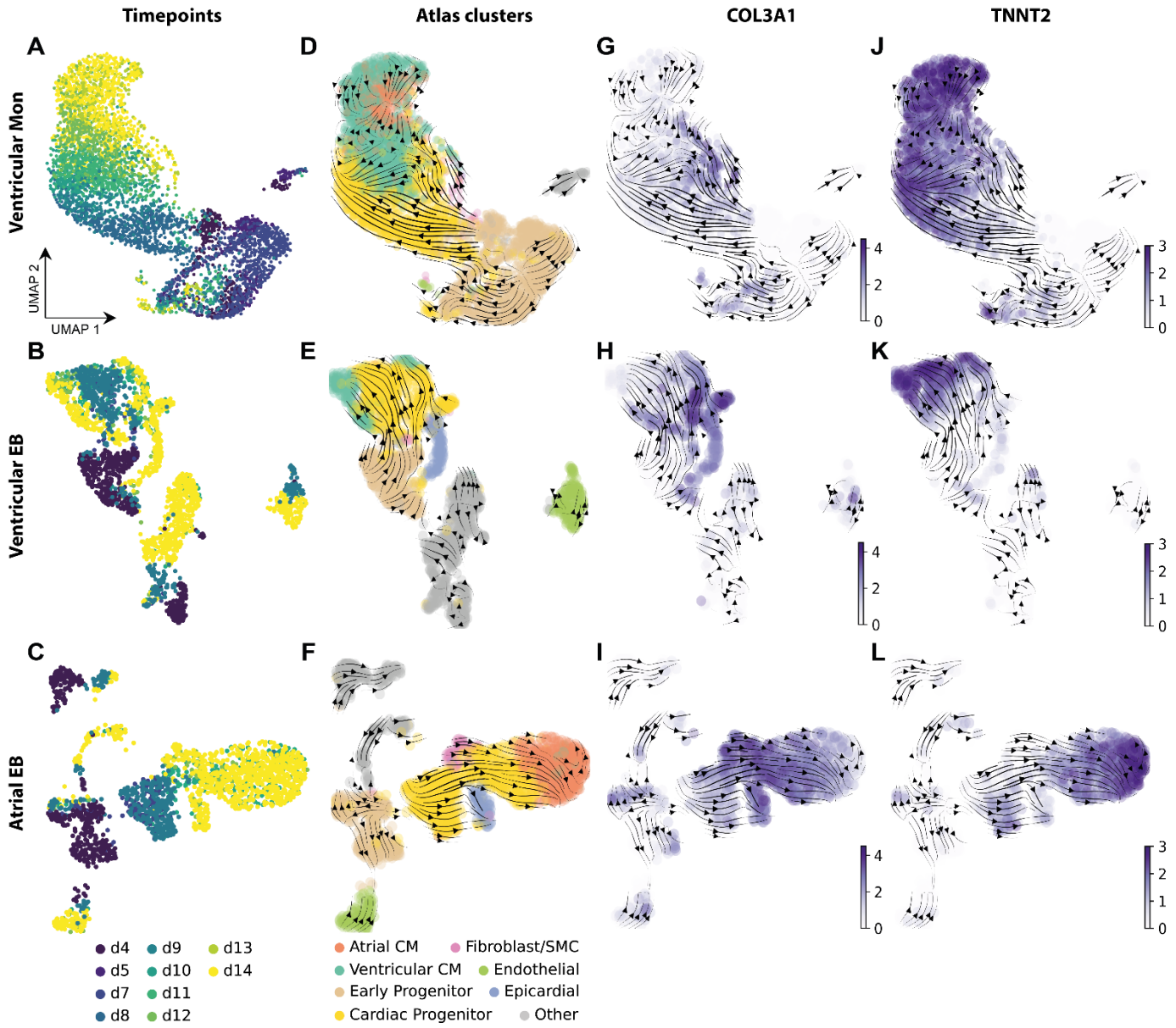


**Figure 2. Cardiac progenitor differentiation trajectories in EB and monolayer cultures.**

UMAP representations of early time point (day 4 to day 14) subsets of the atlas per culture protocol (top, middle and bottom row representing respectively the vCM monolayer, ventricular EB, and atrial EB protocols).

(A-C) UMAPs labelled with time points (d4-d14, days of differentiation).

(D-F) UMAPs labelled with atlas cell states (cf. Fig. 1D and Supplementary Fig. S4C).

(G-I) and (J-L) UMAPs with the expression values of respectively *COL3A1* and *TNNT2*.

Panels (B-L) additionally show arrows for cell state dynamics predicted by RNA velocity (Methods) based on exonic and intronic reads (proxies for respectively mature and nascent RNA).

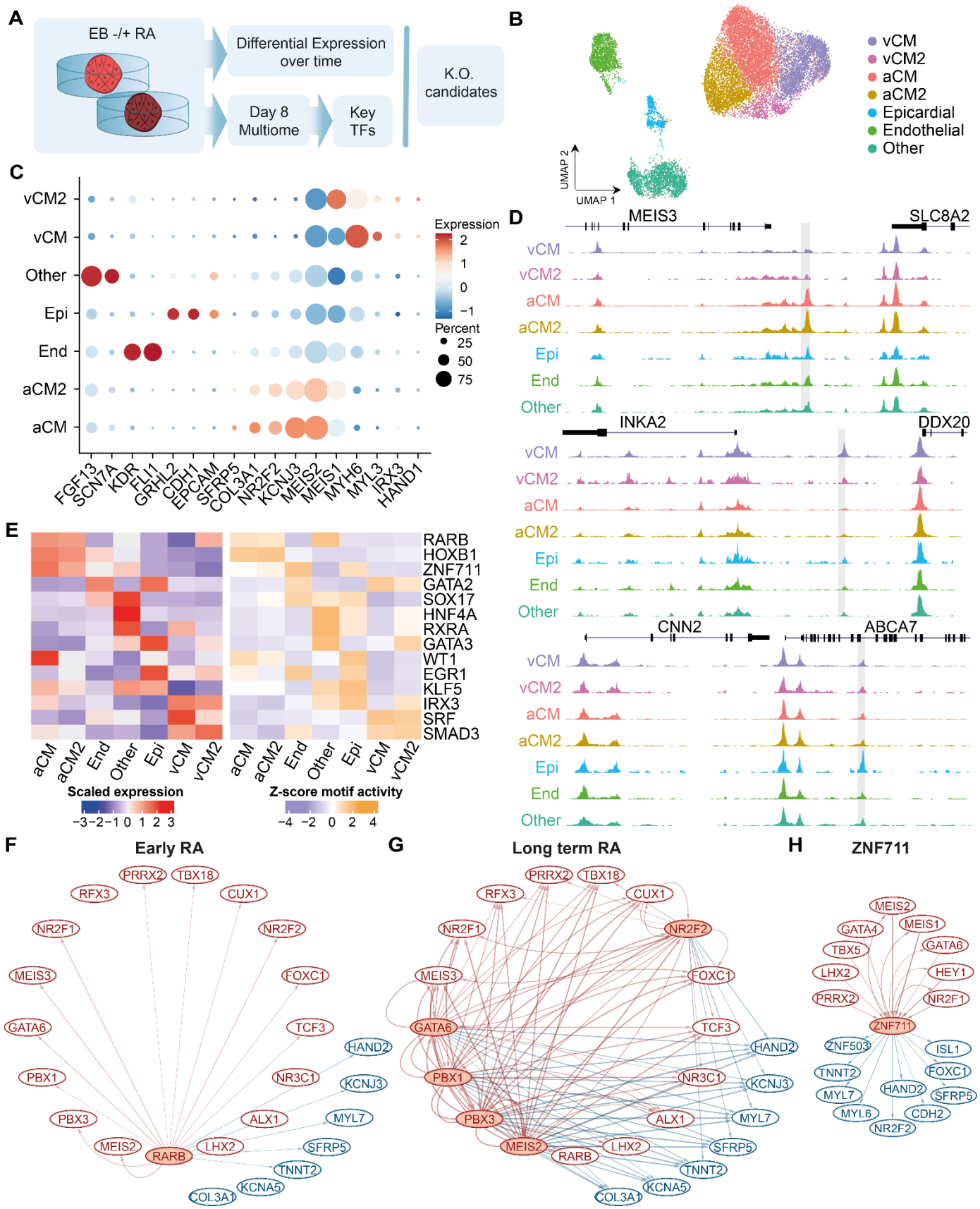


**Figure 3. Identification of transcriptional regulators of the atrial fate with multiome data.**

(A) Schematic overview of the approach to select transcription factors (TFs) of interest in the +RA/non-RA-treated cultures.

(B) UMAP representation of the multiome data from a day 8 embryoid culture (EB) directed towards the atrial and ventricular lineage. Dimensionality reduction and clustering of the cells was performed on the single-cell RNA-seq fraction of the data.

(C) Scaled marker gene expression levels over the different cell states.

(D) Cluster pseudobulk signals of the scATAC-seq data, zoomed in on the three different loci in Genome Browser view, where a differentially accessible peak was identified enriched in the atrial (top), ventricular (middle) and epicardial (bottom) cluster, between the *MEIS3* and *SLC8A2* gene (top), *INKA2* and *DDX20* gene (middle) and within the *ABCA7* gene (bottom). The grey box highlights a 200bp peak identified as differential in signal across the clusters. Black boxes within the genes indicate exons.

(E) Motif enrichment as identified by Maelstrom analysis on the peaks shown in full in Supplemental Table S1A-B. Left heatmap shows expression levels of binding TFs, right heatmap the linked motif activity as inferred with motif analysis.

(F-G) Differential network of the aCM over the vCM cluster, as predicted by scANANSE. Top 20 most influential transcriptional regulators (red) are shown, including 7 markers of interest (blue). Nodes in the network are highlighted for the temporal expression with (F) showing the Early RA responding gene RARB and the connections to its targets and (G) the Long-term RA responding genes and their target interactions. The highlighting for the presence of the regulators in one of the RA gene subsets as presented in Supplemental Fig. S8H.

(H) Subset of the aCM network for gene of interest ZNF711, with a selection of influential factors identified in aCM differential network (red) and targets of interest (blue).

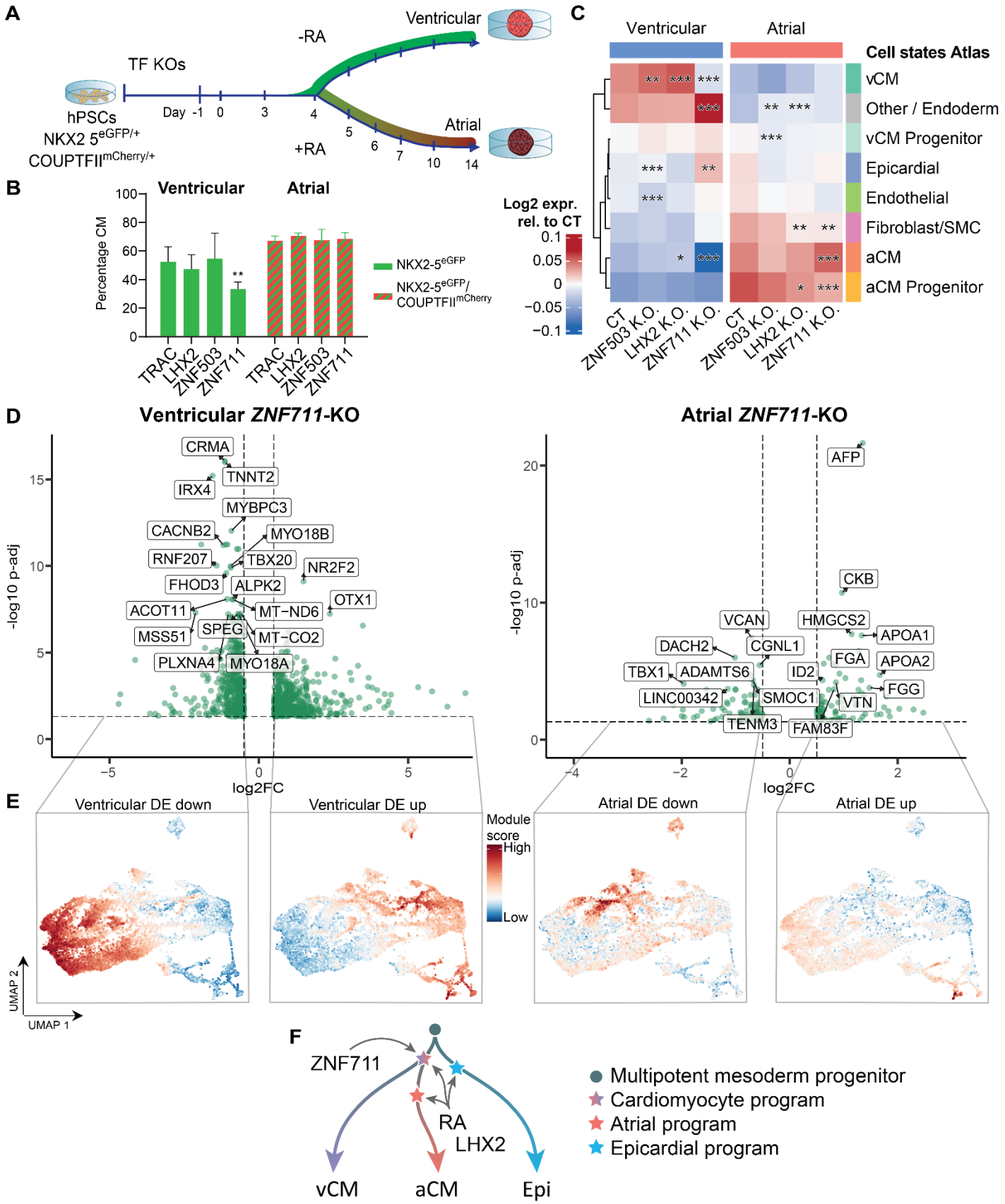


**Figure 4. Knock-out experiments for LHX2, ZNF711 and ZNF503.**

(A) Experimental set-up for the transcription factor (TF) knockout (KO) experiments.

(B) Percentages of cardiomyocytes (CM) per KO, for non-RA-treated (ventricular, left green bars) and +RA-treated (atrial, green and red bars) conditions, control (CT; *TRAC* gene CRISPR control) measured in cells positive for the CM reporters NKX2-5 in non-RA-treated and NR2F2 (aCM) in +RA-treated cultures.

(C) Averaged expression scores within the *LHX2*-KO and *ZNF711*-KO compared to control. The top 200 marker genes per cell type were determined in day 14 embryoid body cells from non-RA and +RA conditions, and used to average the expression levels in the CT and KO samples. Averaged expression scores are divided by the average score of both CT for the same cell type.

(D) Volcano plot of the differentially expressed (DE) genes of the *ZNF711*-KO cells cultured towards ventricular cardiomyocytes (non-RA, left) and atrial cardiomyocytes (+RA, right) (adjusted p-value < 0.05). Top hits with the lowest adjusted p-value are indicated with text labels. The vertical dotted line indicates a threshold of |log2FC| > 0.5 and the horizontal dotted line |-log10P-value| < 0.05.

(E) The *in vitro* atlas (Fig. 1) labelled with compound gene expression levels (module scores) based on the gene groups from left to right: non-RA downregulated (log2FC < 0), non-RA downregulated (log2FC > 0), +RA downregulated and +RA upregulated genes, based on significance (p-adjusted < 0.05) after *ZNF711*-KO. CT = control, aCM = atrial, vCM = ventricular, RA = retinoic acid, DE = differentially expressed, log2FC = log2 (expression fold change between KO and CT).

(F) Requirements for balanced lineage commitment of progenitors to epicardial cells, atrial and ventricular cardiomyocytes by the concerted action of *ZNF711*, *LHX2* and retinoic acid.

## SUPPLEMENTARY FIGURES

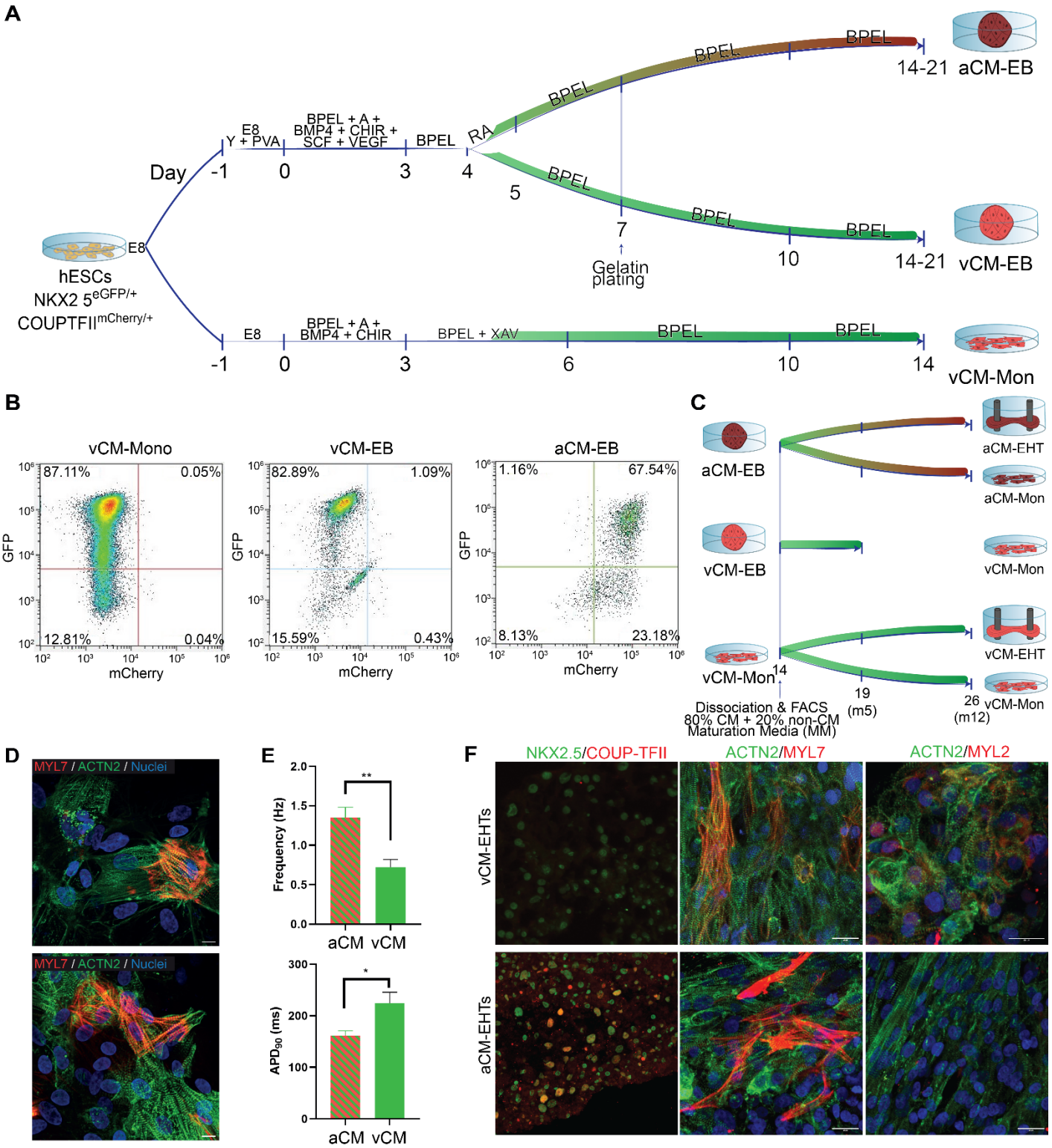


**Supplementary Figure S1. Atrial and ventricular differentiation protocols and CM characterization**.

(A) Detailed overview of the differentiation protocols from hPSC towards atrial or ventricular embryonic bodies (aCM-EBs, vCM-EBs, respectively) or ventricular monolayers (vCM-Mon). Abbreviations: E8 = Essential 8 media; BPEL = Bovine Serum Albumin Polyvinylalchohol Essential Lipids media; A = Activin A; BMP4 = Bone Morphogenetic protein 4; CHIR = Chir99021; SCF = Stem Cell Factor; VEGF = Vascular Endothelial Growth Factor; RA = retinoic acid analog; XAV = xav939; m = day in maturation medium.

(B) Representative flow cytometry plots depicting the differentiation efficiency of the resultant cardiomyocytes at day 14 from each of the differentiation protocols used in (A), using the reporter line NKX-2.5$^{eGFP+/-}$-COUP-TFII$^{mCherry+/-}$. Atrial CMs are both GFP and mCherry positive while ventricular CMs only GFP positive.

(C) Schematic overview of the protocol used at day 14 to generate EHTs and monolayer controls per culture type. Note from vCM-EB only monolayers were generated since EHTs from vCM-Mon were more efficient to generate. m5-m12 = day 5-12 in maturation medium (day 14-26; EHT and monolayer only).

(D) Additional immunohistochemistry of general cardiomyocyte markers MYL7 and ACTN2 in day 21 vCM-EBs (top) and aCM-EBs (bottom). Scale bar = 20 µm.

(E) Frequency (top) and action potential duration at 90% of repolarization (APD90) (bottom) of aCMs and vCMs EBs at day 14, determined by FluoVolt voltage sensitive dye. Data are mean ± s.e.m. Two-tailed Student's t-test. *$p < 0.05$; **$p < 0.01$. (n = 6 EBs from 3 batches of differentiation).

(F) Representative confocal images of ventricular and atrial EHTs (aCM-EHTs, vCM-EHTs, respectively) stained for NKX-2.5, COUP-TFII, ACTN2, MYL7 and MYL2 confirming their lineage identity. Scale bar = 20 µm.

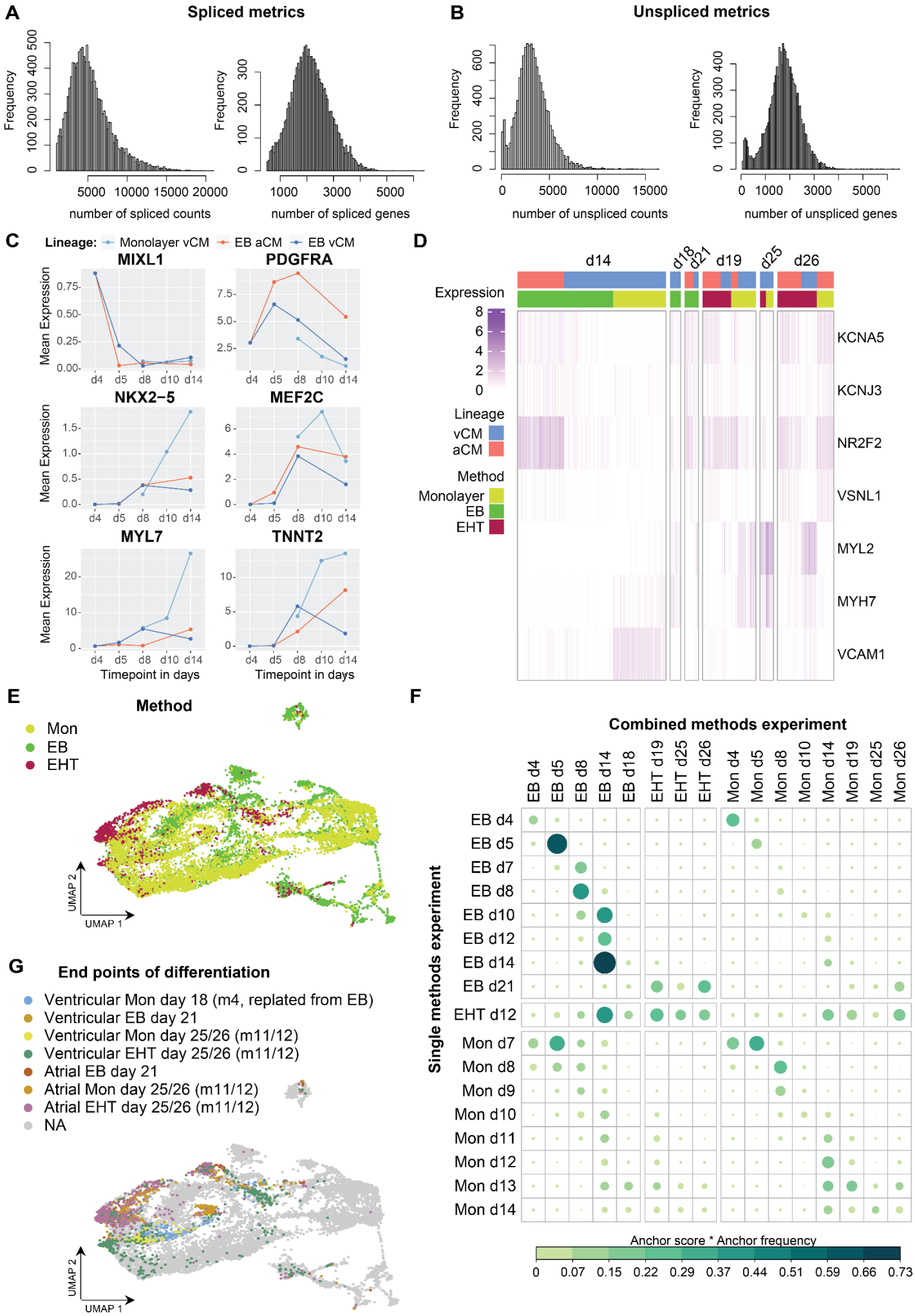
A
Spliced metrics
Frequency
number of spliced counts
number of spliced genes
B
Unspliced metrics
number of unspliced counts
number of unspliced genes
C
Lineage: Monolayer vCM EB aCM EB vCM
MIXL1
PDGFRA
NKX2−5
MEF2C
MYL7
TNNT2
Mean Expression
Timepoint in days
D
d14
d18
d21
d19
d25
d26
Expression
Lineage
vCM
aCM
Method
Monolayer
EB
EHT
KCNA5
KCNJ3
NR2F2
VSNL1
MYL2
MYH7
VCAM1
E
Method
Mon
EB
EHT
UMAP 2
UMAP 1
F
Combined methods experiment
Single methods experiment
Anchor score * Anchor frequency
G
End points of differentiation
Ventricular Mon day 18 (m4, replated from EB)
Ventricular EB day 21
Ventricular Mon day 25/26 (m11/12)
Ventricular EHT day 25/26 (m11/12)
Atrial EB day 21
Atrial Mon day 25/26 (m11/12)
Atrial EHT day 25/26 (m11/12)
NA

**Supplementary Figure S2. Single-cell RNA-sequencing dataset.**

(A-B) Histogram showing the frequency of cells counted in the dataset after quality filtering with (A) spliced (exonic) or (B) unspliced (intronic) reads, summarized as read counts (left) and detected genes (right) per cell (x-axis).

(C) Combined time point expression of mesoderm (*MIXL1*), cardiac progenitor (*PDGFRA*, *MEF2C*, *NKX2-5*) and cardiomyocyte (*MYL7*, *TNNT2*) marker genes in each differentiation protocol (ventricular Mon, atrial EB, ventricular EB). Time points shown only include those with at least one replicate between the experiments.

(D) Heatmap representation of atrial and ventricular markers for evaluation of lineage identity in atrial (salmon-red) and ventricular (blue) cultures from day 14 to day 26. Yellow-green, green and carmine-red indicate monolayer, embryoid body and engineered heart tissue respectively.

(E) UMAP representation of the integrated dataset as shown in Fig. 1C-D, cells labelled for the method (top).

(F) Dotplot visualizing the frequency and score of mutual nearest neighbors (integration anchors) between the culture experiments, columns show the samples in one experiment where all methods were cultured in parallel, the rows indicated separate experiments for each of the culture methods. Size and color of the dots represents the product of anchor score and anchor frequency.

(G) UMAP representation of the integrated dataset as shown in Fig. 1C-D, cells labelled for the end points of differentiation for each of the different methods (full protocol of differentiation is shown in Figure 1A, Supplementary Fig. S1A,C). m4-m11-m12 = day 4-11-12 in maturation medium (day 18-25-26; EHT and monolayer only).

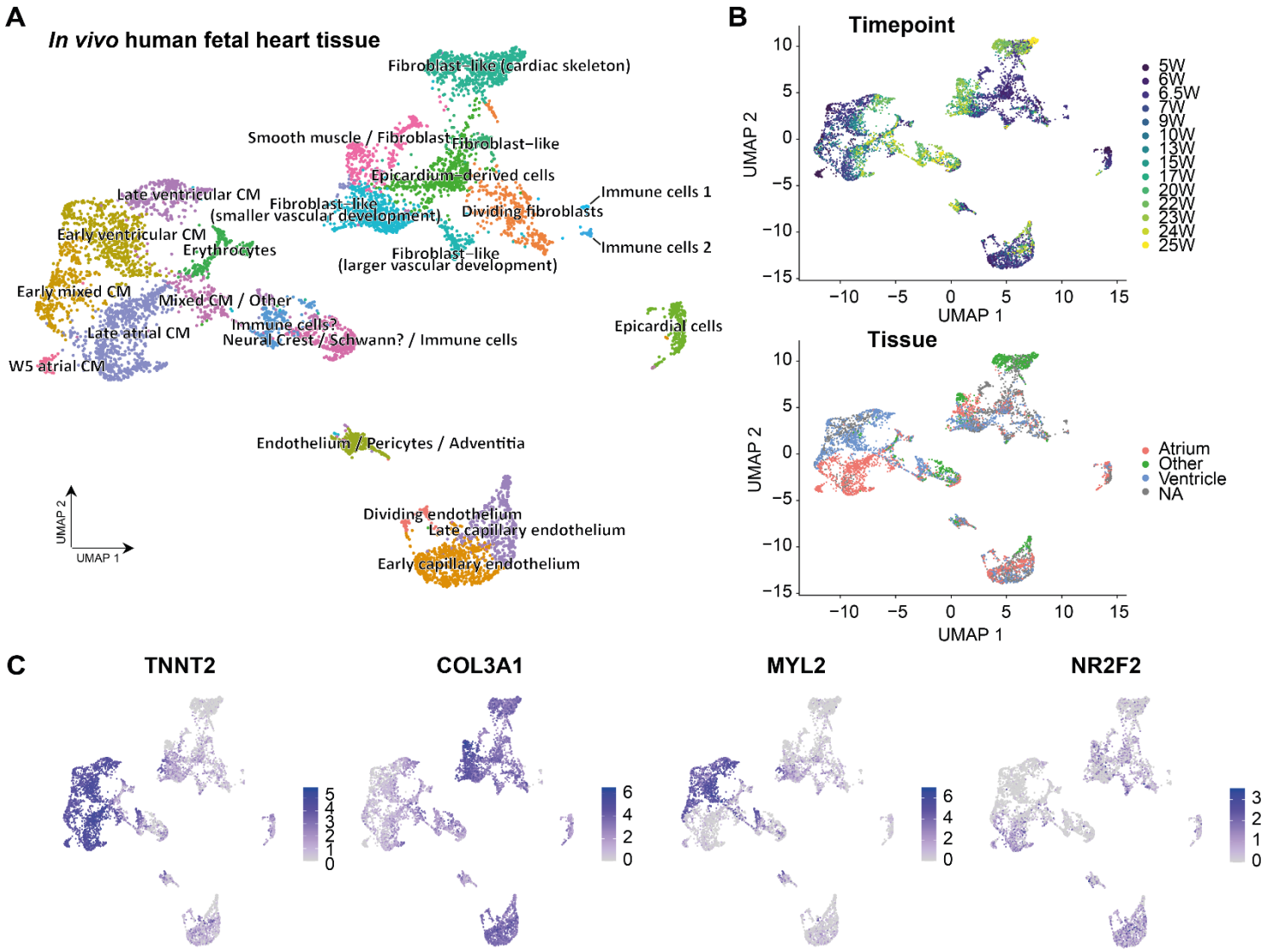


**Supplementary Figure S3. Cell types of the human fetal heart.**

(A) Integrated scRNA-seq datasets of human fetal heart tissue from Cui et al. (2019) and Asp et al. (2018), labelled with extended annotation based on the cell types annotated in the Asp et al. dataset.

(B) UMAP representation as shown in (B) labelled with time point (top) and tissue (bottom) of harvest where this information was provided (w, weeks after conception).

(C) Gene expression of known markers *TNNT2* (general cardiac muscle marker), *MYL2* (ventricular cardiomyocyte marker), *NR2F2* (atrial cardiomyocyte marker), and *COL3A1*.

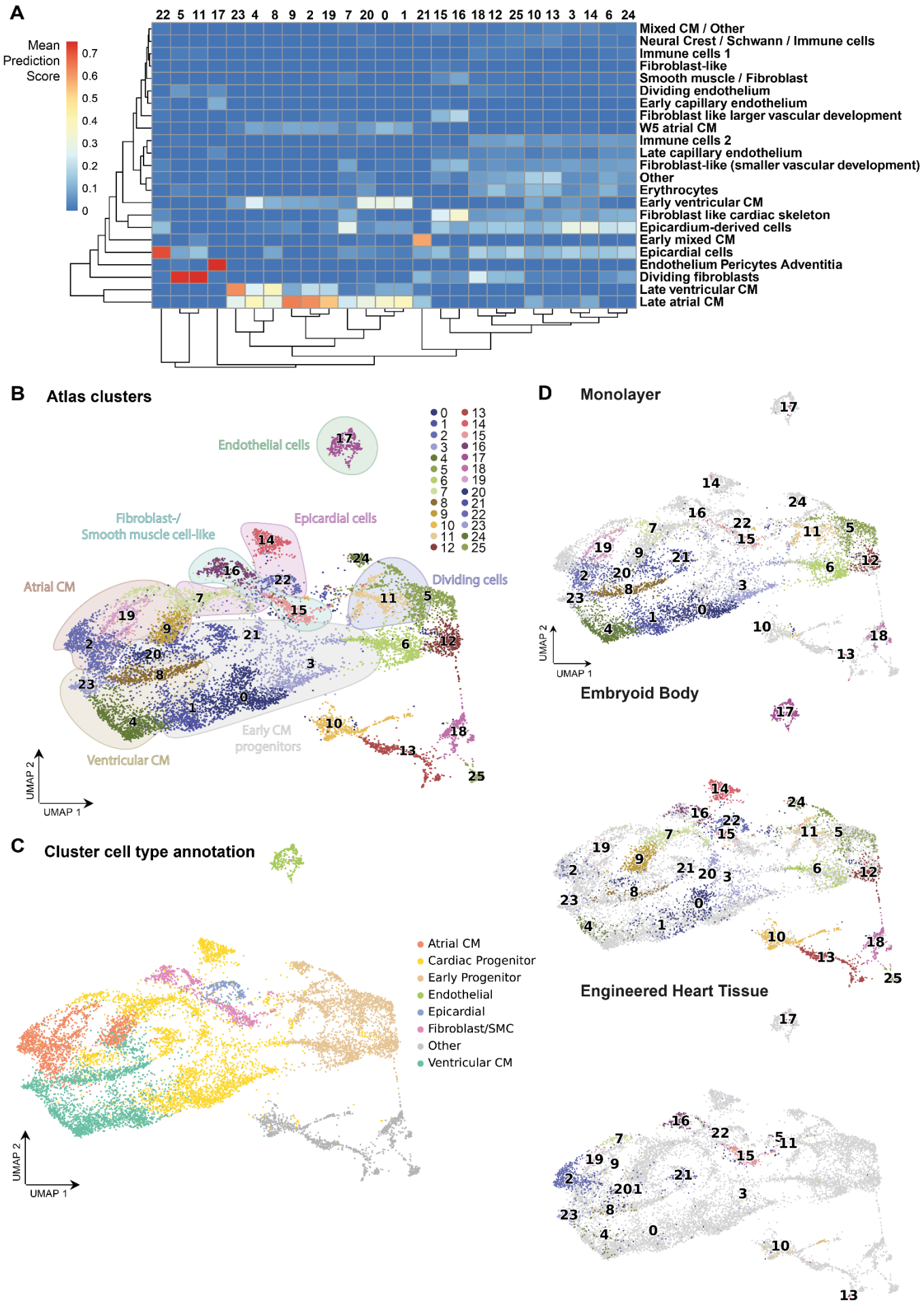


**Supplementary Figure S4. Annotating the temporal single-cell atlas.**

(A) Heatmap with predicted fetal cell types from Figure S3 (rows) for each of the atlas clusters from Figure 1C and S3A (columns). Multiple late time point clusters (day 14 and older) from the ventricular and atrial lineage, show most similarity to in vivo vCM and aCM clusters, respectively. Cluster 22 matched best with epicardial and cluster 17 with endothelial cells. Early clusters were similar to proliferating fibroblasts (cluster 5 and 11).

(B) UMAP representation of the atlas with cluster labelling, colored stains show the annotation process based on the scoring in (A). (C) UMAP representation of the atlas with cell state annotation.

(D) UMAP representation of the full atlas, with coloring of the clusters as shown in (B), separated per culture method. Cells in light grey fall outside of the culture method of focus.

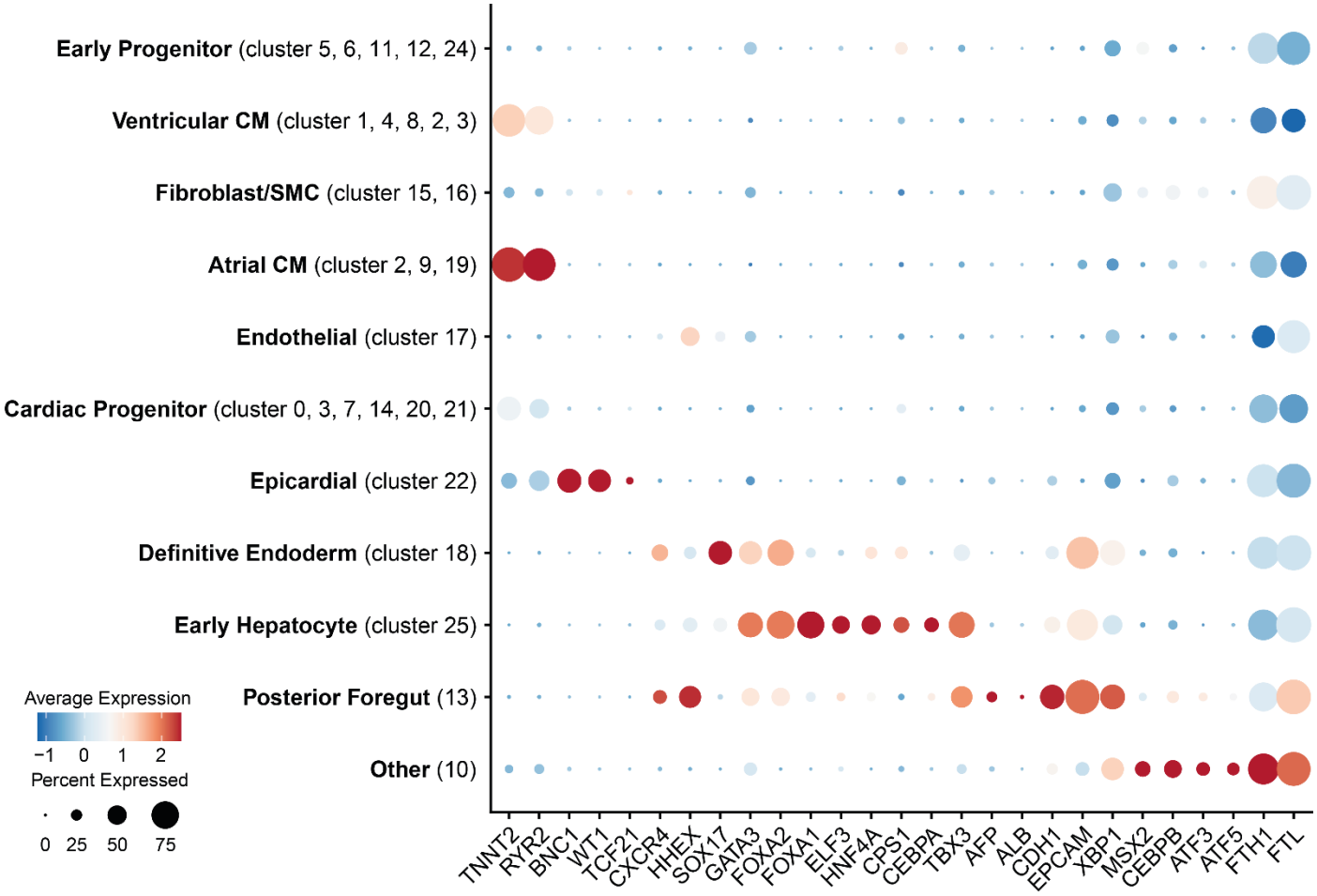


**Supplementary Figure S5.**

Dotplot showing marker genes for the different clusters: general cardiomyocyte *TNNT2*, *RYR2*; epicardial *BNX1*, *WT1*, *TCF21*; and markers for definitive endoderm (*SOX17*, *CXCR4* (or *CD184*), *GATA3*, *FOXA1*, *FOXA2*), early hepatocyte (*FOXA1*, *ELF3*, *HNF4A*, *CPS1*, *CEBPA*, *TBX3*, *AFP*, *ALB*), (posterior) foregut (*ELF3*, *HHEX*, *CDH1*, *EPCAM*), and marker genes found in the Other cluster (*MSX2*, *CEBPB*, *ATF3*, *ATF5*, *FTH1*, *FTL*).

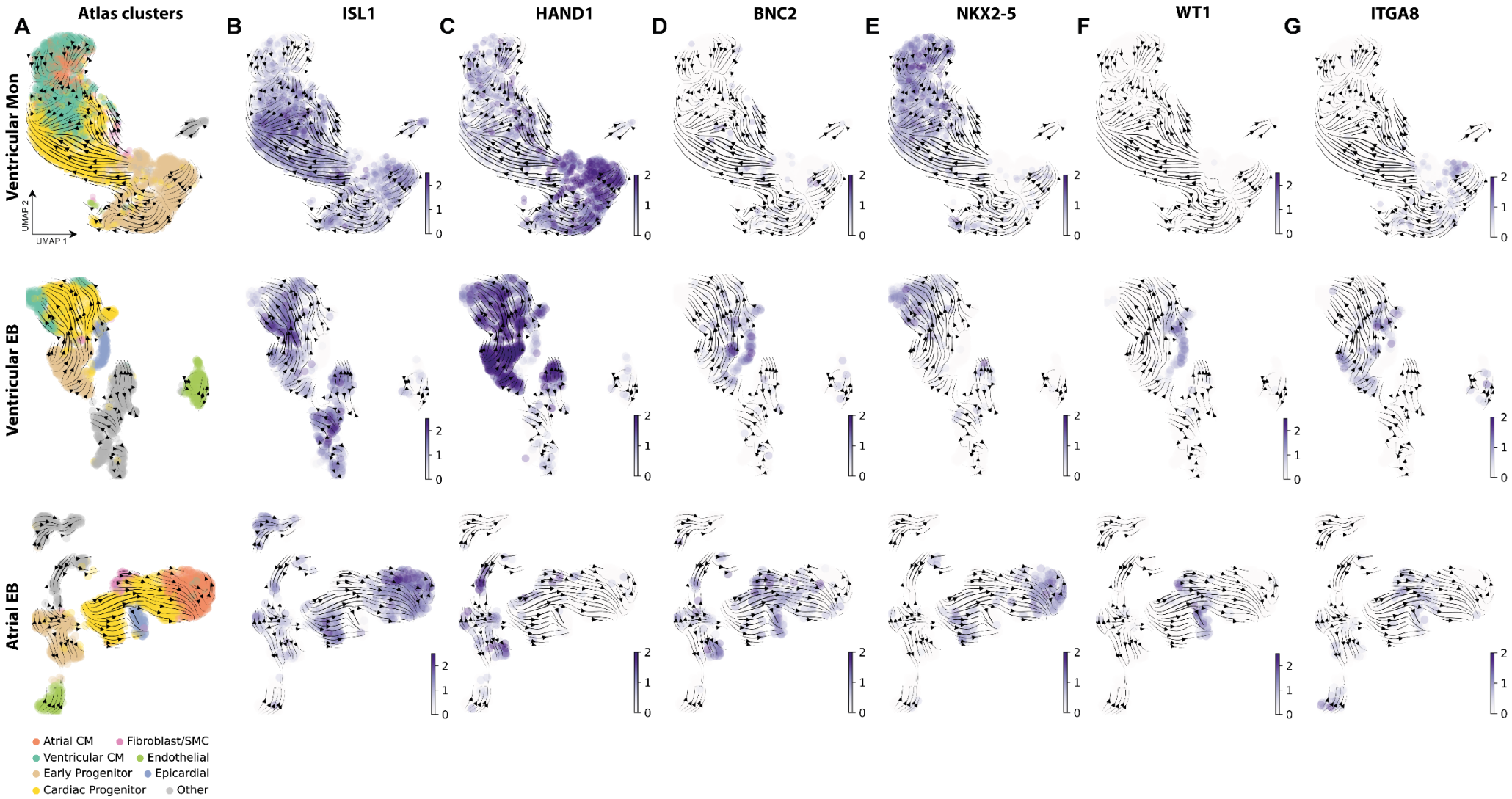


**Supplementary Figure S6: Early trajectories with SHF and early CM markers ISL1 and NXK2-5 and (pre-)epicardial marker expression.**

Per culture protocol UMAP representation with ventricular monolayer culture (top), ventricular embryoid body (EB) (middle) and atrial EB (bottom) labeled for cell types (A) and expression levels of SHF marker *ISL1* (B), epicardial marker *WT1* (C) and genes expressed in pre-epicardial cells *HAND1* (D), *BNC2* (E), *NKX2-5* (F), as well as the new epicardial surface marker *ITGA8* (G) (Zawada et al., 2023).

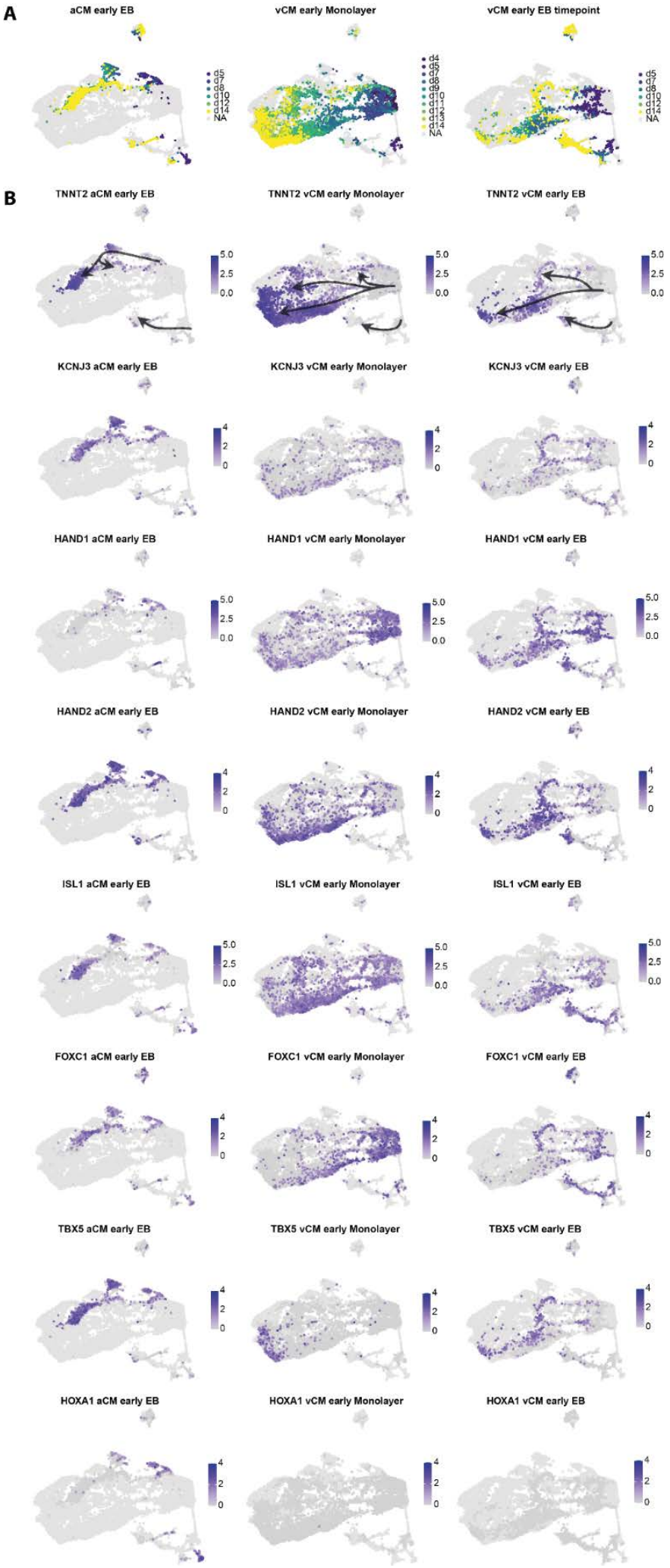
A
aCM early EB
vCM early Monolayer
vCM early EB timepoint
d5
d7
d8
d10
d12
d14
NA
d4
d5
d7
d8
d9
d10
d11
d12
d13
d14
NA
B
TNNT2 aCM early EB
TNNT2 vCM early Monolayer
TNNT2 vCM early EB
KCNJ3 aCM early EB
KCNJ3 vCM early Monolayer
KCNJ3 vCM early EB
HAND1 aCM early EB
HAND1 vCM early Monolayer
HAND1 vCM early EB
HAND2 aCM early EB
HAND2 vCM early Monolayer
HAND2 vCM early EB
ISL1 aCM early EB
ISL1 vCM early Monolayer
ISL1 vCM early EB
FOXC1 aCM early EB
FOXC1 vCM early Monolayer
FOXC1 vCM early EB
TBX5 aCM early EB
TBX5 vCM early Monolayer
TBX5 vCM early EB
HOXA1 aCM early EB
HOXA1 vCM early Monolayer
HOXA1 vCM early EB
5.0
2.5
0.0
4
2
0

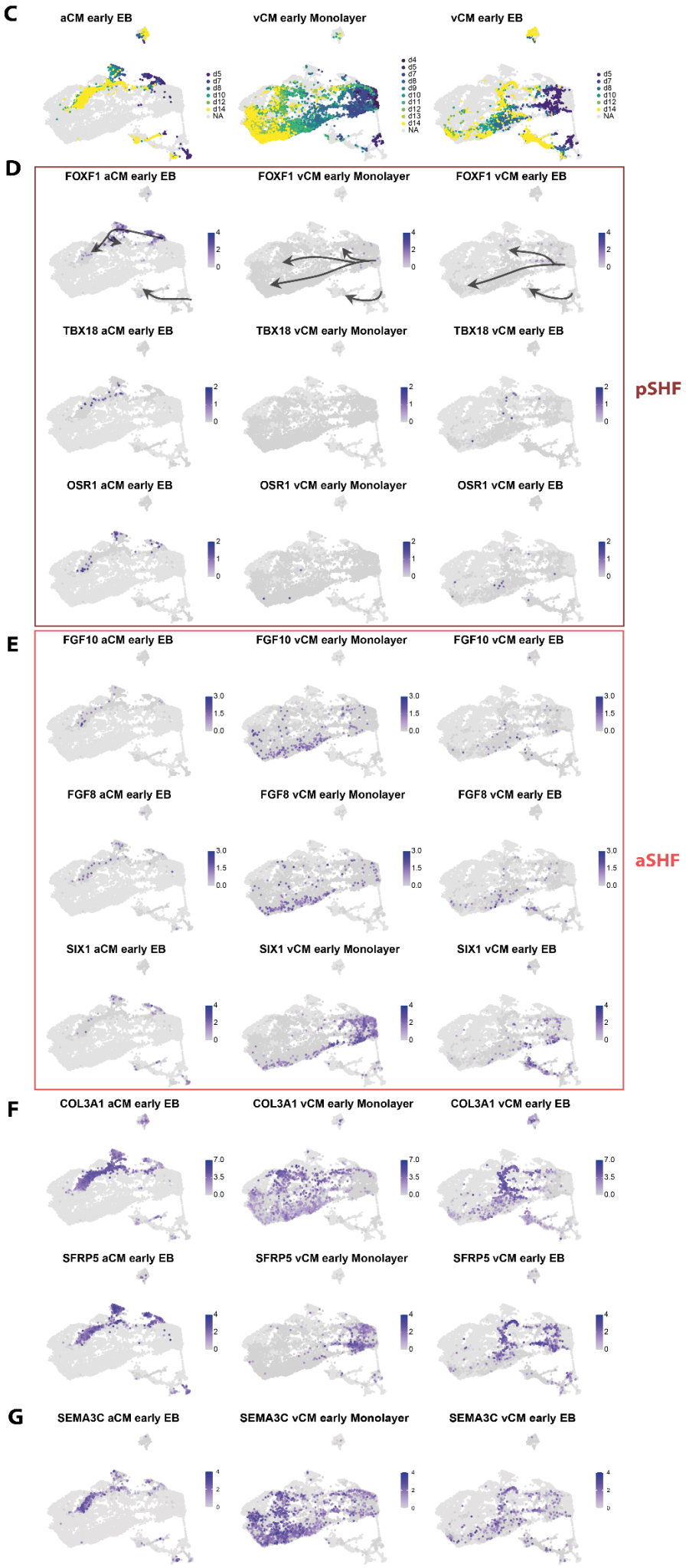
C
aCM early EB
vCM early Monolayer
vCM early EB
d5
d7
d8
d10
d12
d14
NA
d4
d5
d7
d8
d9
d10
d11
d12
d13
d14
NA
D
FOXF1 aCM early EB
FOXF1 vCM early Monolayer
FOXF1 vCM early EB
TBX18 aCM early EB
TBX18 vCM early Monolayer
TBX18 vCM early EB
OSR1 aCM early EB
OSR1 vCM early Monolayer
OSR1 vCM early EB
pSHF
E
FGF10 aCM early EB
FGF10 vCM early Monolayer
FGF10 vCM early EB
FGF8 aCM early EB
FGF8 vCM early Monolayer
FGF8 vCM early EB
SIX1 aCM early EB
SIX1 vCM early Monolayer
SIX1 vCM early EB
aSHF
F
COL3A1 aCM early EB
COL3A1 vCM early Monolayer
COL3A1 vCM early EB
SFRP5 aCM early EB
SFRP5 vCM early Monolayer
SFRP5 vCM early EB
G
SEMA3C aCM early EB
SEMA3C vCM early Monolayer
SEMA3C vCM early EB

**Supplementary Figure S7: Early trajectory expression patterns.**

(A) Atlas UMAP representation labelled with time point of harvest per culture protocol, cells from other protocols in the atlas are shown in light grey (NA).

(B) Expression levels of genetic markers for the cardiomyocytes (*TNNT2*), atrial CM (*KCNJ3*), first heart field (*HAND1*), second heart field (*HAND2*, *ISL1*, *FOXC1*, *TBX5*).

(C) Same representation as in (A). UMAP labelled with time point of harvest per culture protocol, cells from other protocols in the atlas are shown in light grey (NA).

(D) Expression levels of genetic markers for the posterior second heart field (pSHF).

(E) Expression levels of genetic markers for the anterior second heart field (aSHF).

(F) Expression levels of *SFRP5* and *COL3A1*, which showed elevated co-expression in the non-CM branches of the UMAP, where *SFRP5* was downregulated and to a lower extent *COL3A1* in the ventricular cardiomyocyte branch (middle and right), whereas both remain upregulated in atrial CM differentiation (left).

(G) Expression levels of *SEMA3C* marker of aSHF-derived ventricular cardiomyocytes.

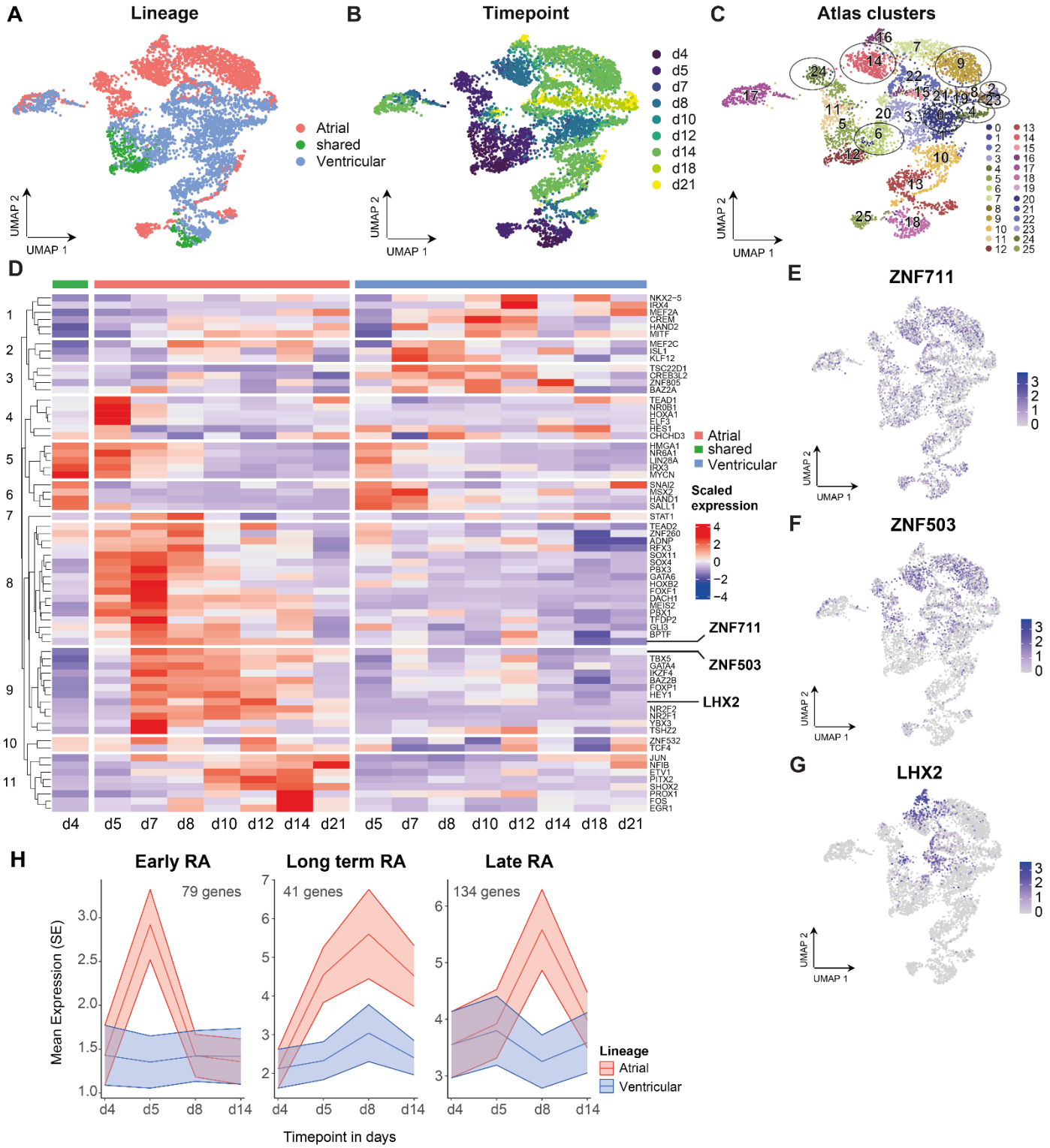


**Supplementary Figure S8. Transcription factor analysis in the embryoid body (EB) atlas subset.**

(A) UMAP representation of EB subset of the atlas, cells labelled with the lineage they were cultured towards (left) and the time point the cells were harvested (right).

(B) UMAP with circles outlining the differential gene analysis between the lineages performed on atlas clusters in trajectory to aCM and vCM. Comparisons were performed between cluster 24 and 6, cluster 14 and 0, cluster 9 and 4, and between cluster 2 and 23 were made.

(C) Heatmap showing the results of differential expression analysis between early and late cardiomyocyte clusters, outlined in (B), across the two lineages within the EB dataset.

(D) Highlighted hits of interest from (B) visualized over the UMAP representation of the EB subset.

(E) Average expression levels over time per gene set which was found differentially upregulated in atrial versus ventricular culture, subdivided into an early RA-responsive (left), a long-term RA-responsive (middle) and late RA-

responsive subset (right) (Methods). d = day of culture, day 4 is shared between the lineages and day 5 the first day after administration of RA in the atrial culture.

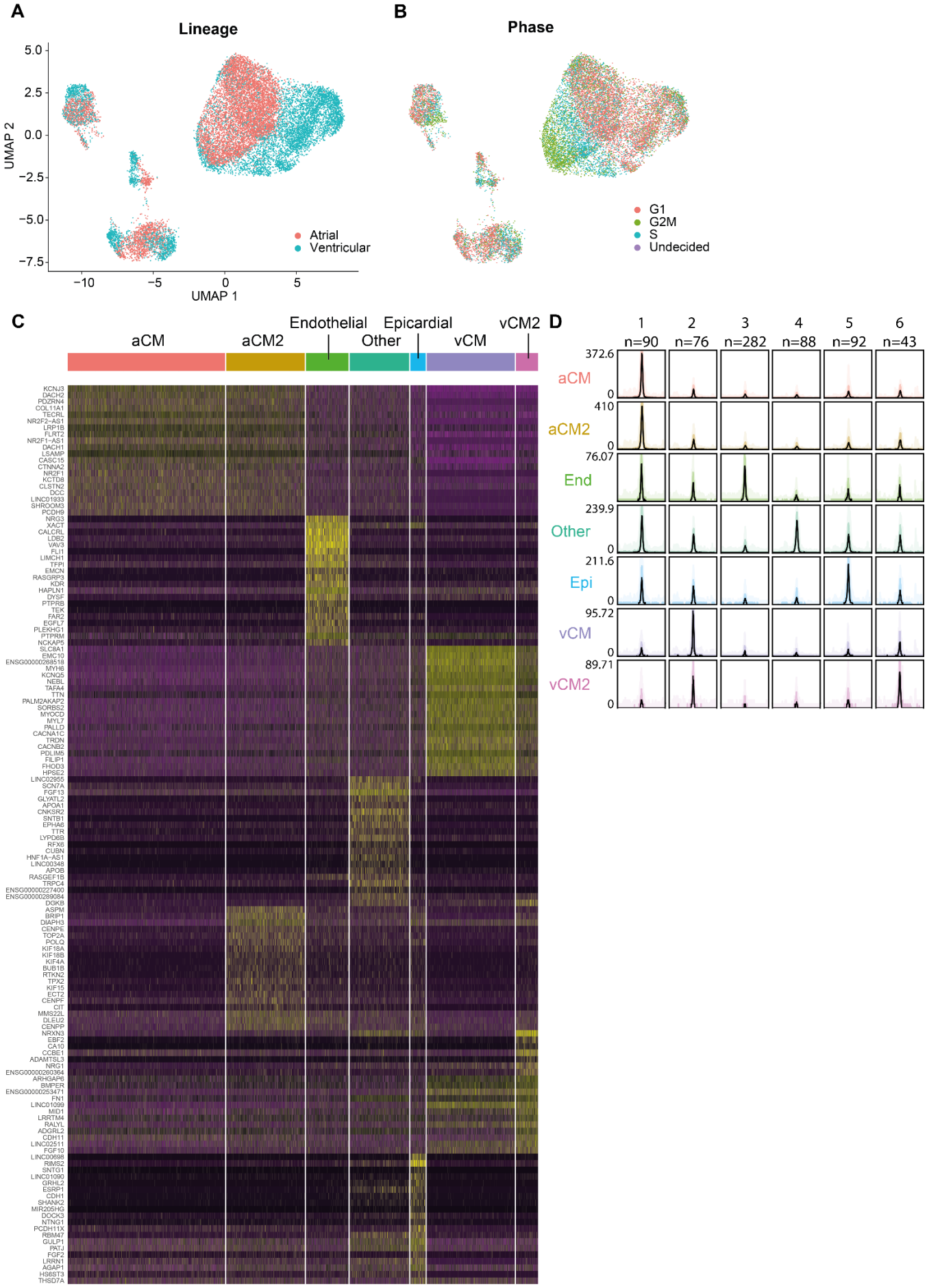

**Supplementary Figure S9. Cluster identification and patterns of gene expression and chromatin accessibility in the multiome dataset.**

(A-B) UMAP representation from Figure 3c with labels of the lineage they were cultured towards (A) and the predicted cell cycle phase (B).

(C) Heatmap visualizing expression levels of top 20 genetic markers, called per cell type.

(D) Chromatin accessibility patterns per cell type in the multiome dataset with a bandplot showing a graph illustration of differentially accessible peaks per cluster. These peaks were used for motif analysis (Supplementary Table S1A-B).

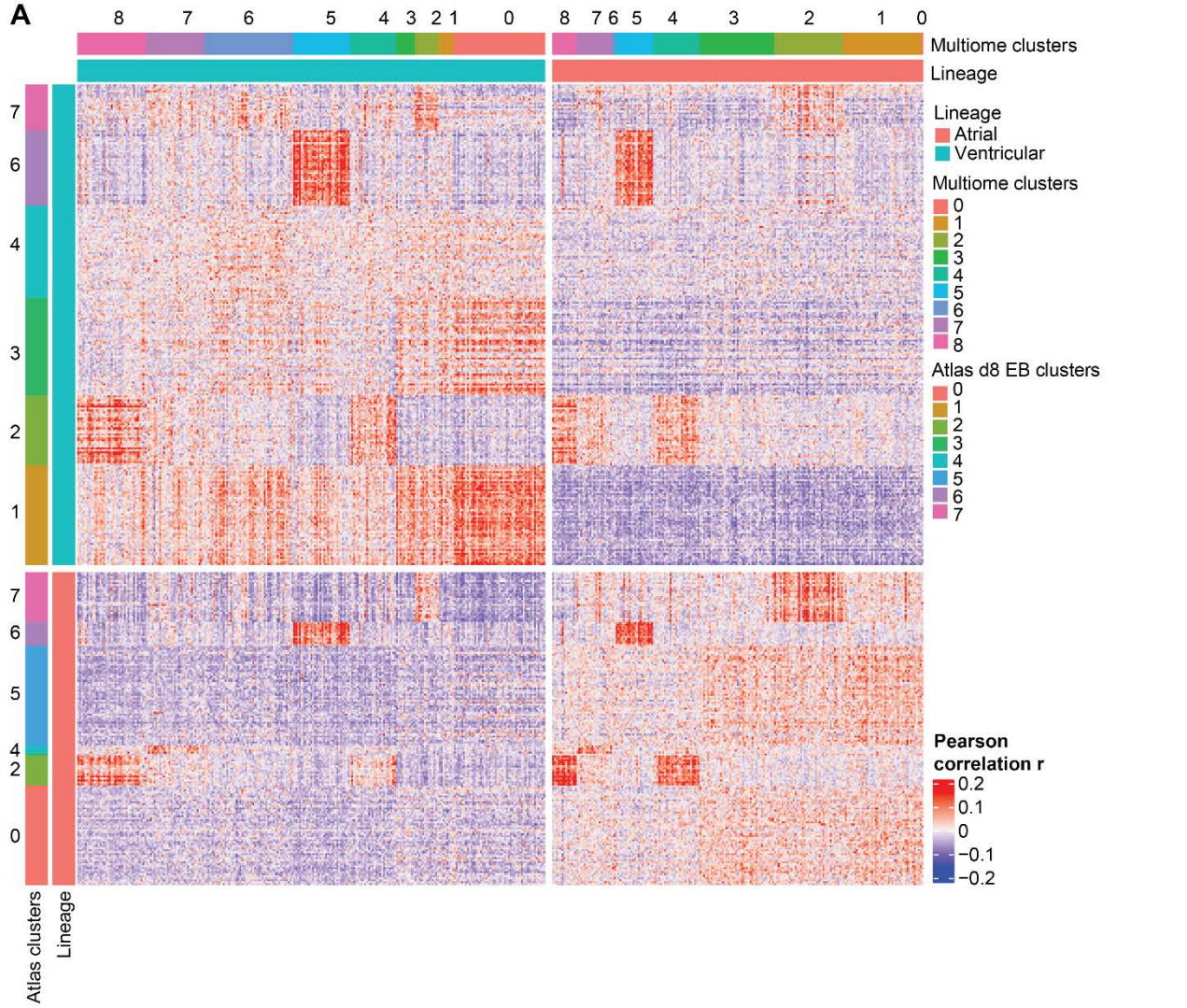
A
Multiome clusters
Lineage
Lineage
Atrial
Ventricular
Multiome clusters
Atlas d8 EB clusters
Pearson correlation r
0.2
0.1
0
−0.1
−0.2
Atlas clusters
Lineage

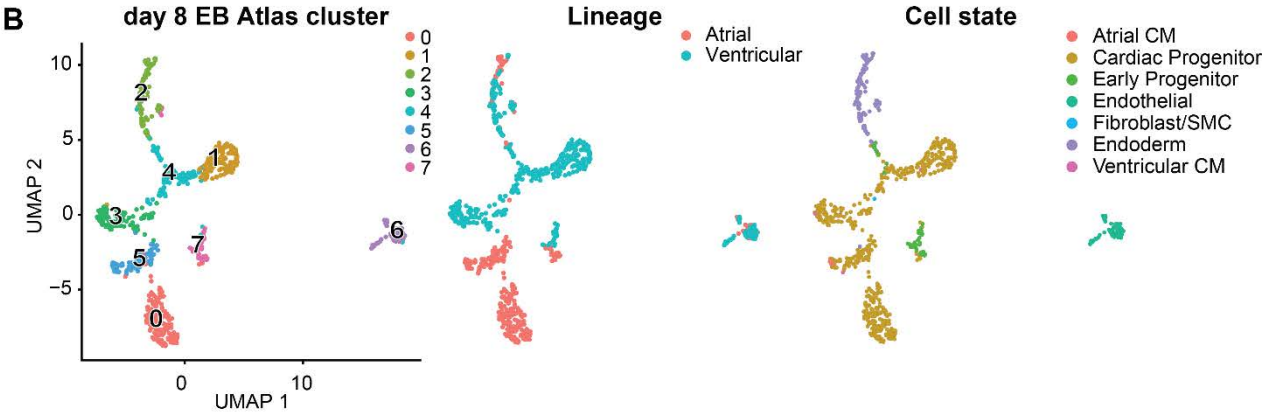
B
day 8 EB Atlas cluster
Lineage
Atrial
Ventricular
Cell state
Atrial CM
Cardiac Progenitor
Early Progenitor
Endothelial
Fibroblast/SMC
Endoderm
Ventricular CM
UMAP 2
UMAP 1

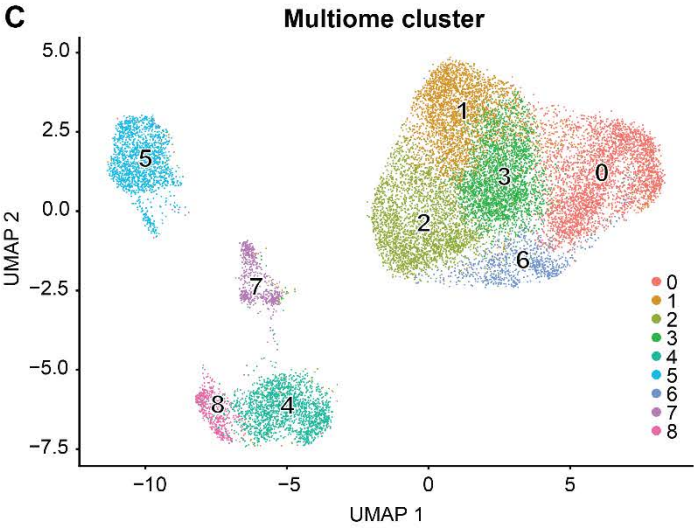
C
Multiome cluster
UMAP 2
UMAP 1

**Supplementary Figure S10: Correlations between day 8 EB subset of the temporal Atlas and day 8 multiome data.**

(A) Correlation heatmap with random subsets of 1,000 cells per cluster in the multiome dataset for the columns and all cells per cluster of the atlas dataset in the rows, additionally separated per lineage.

(B) UMAP shown with clusters called for the d8 EB subset of the atlas (left), labelled for lineage origin (middle) and labeled for cell types as annotated in the atlas (right). (C) UMAP representation of the multiome dataset labelled with the cluster numbers.

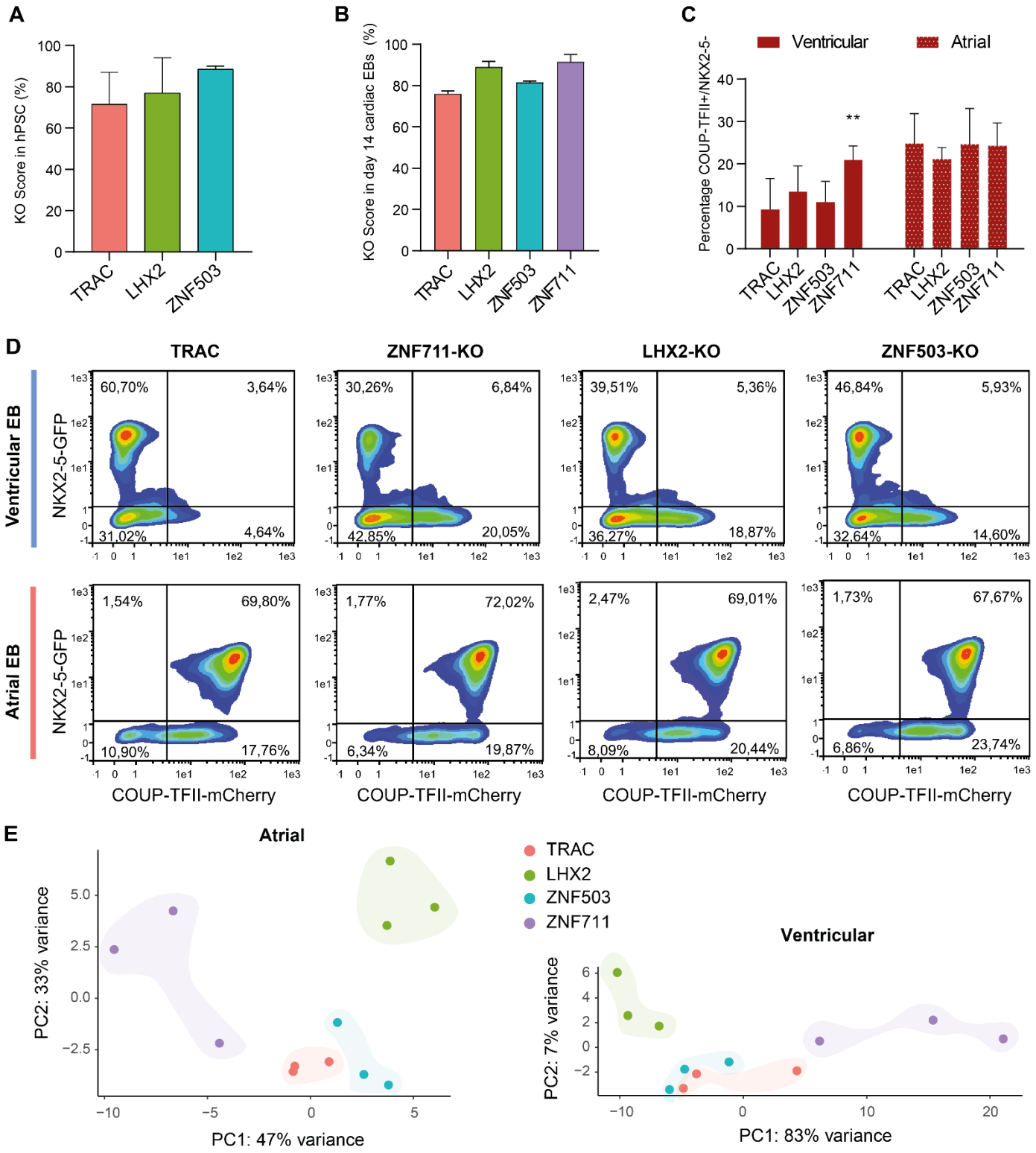


**Supplementary Fig S11 Transcription factor knockout experiment read-out.**

(A) Knockout (KO) efficiency per target at the start of differentiation, TRAC is used as a negative control.

(B) KO efficiency per target after differentiation measured at day 14 of embryoid body (EB) culture averaged over both lineages.

(C) Percentages of COUP-TFII (or NR2F2)-positive and NKX2-5-negative cells per KO, for non-RA-treated (ventricular, left red bars) and +RA-treated (atrial, red, white-dotted bars) conditions, control (CT; *TRAC* gene CRISPR control) measured in cells positive for the CM reporters NKX2-5 in non-RA-treated and NR2F2 (aCM) in +RA-treated cultures.

(D) Representative flow cytometry results from panel (C), showing on the y-axis the signal measured for NKX2-5-GFP and on the x-axis the signal measured for COUP-TFII-mCherry, represented with a density plot for each of the control

conditions (TRAC) and KO conditions, cultured with ventricular (non-RA, top row) or atrial (+RA, bottom row) conditions.

(E) PCA on RNA-seq of KO target samples obtained after 14 days of EB differentiation separate for atrial (plus RA; top) and the ventricular lineage (no RA; bottom).